RESEARCH ARTICLE SUMMARY

TISSUE MORPHOGENESIS

Morphogens enable interacting supracellular phases that generate organ architecture

Sichen Yang†, Karl H. Palmquist†, Levy Nathan, Charlotte R. Pfeifer, Paula J. Schultheiss, Anurag Sharma, Lance C. Kam, Pearson W. Miller, Amy E. Shyer*‡, Alan R. Rodrigues*‡

INTRODUCTION: During vertebrate organ morphogenesis, large collectives of cells robustly self-organize to form architectural units (bones, villi, follicles) whose form persists into adulthood. Over the past few decades, mechanisms of organ morphogenesis have been developed predominantly through molecular, genetic, and cellular frameworks. More recently, there has been a resurgence of interest in collective cell and tissue mechanics during organ formation. This approach has amplified the need to clarify and unambiguously link events across biological length scales. Doing so may require reassessing canonical models that continue to guide the field. The most recognized model for organ formation centers around morphogens as determinants of gene expression and morphological patterns. The classical view of a morphogen is that morphogen gradients specify differential gene expression in a distinct spatial order. Because morphogen expression colocalizes with emerging feather and hair follicles, the skin has served as a paradigmatic example of such morphogen prepatterning mechanisms.

RATIONALE: Recent work in the avian skin has shown that genes that are thought to establish molecular prepatterns are not expressed focally before the initiation of feather follicle morphology. Instead, the self-organization of mesenchymal progenitor cells in the dermis initiates morphological patterns and activates morphogen gene expression in emerging follicles. The sufficiency of mesenchymal self-organization for initiating patterns has been demonstrated in ex vivo reconstitution systems in which dermal cells and extracellular matrix can recapitulate the process of regular follicle pattern formation. In this work, we asked, what functional role do morphogens serve if not to establish a pattern of follicles across the skin?

RESULTS: Working in avian skin tissues, we found that the morphogens fibroblast growth factor (FGF) and bone morphogenetic protein (BMP) act just before the follicle buds out of the plane of the skin. Together, these morphogens enable the generation of nested spatial domains within the dermis of the follicle: an FGF-active hemispheric core and a surrounding BMP-active margin. In investigating what roles these morphogens play in these domains, we considered biophysical effects that emerge at the supracellular scale. We measured material properties using techniques such as atomic force microscopy and micropipette aspirations and used custom assays to investigate the effect of these morphogens on supracellular material and mechanical properties. We identified morphogen-enabled supracellular material property differences (e.g., elasticity) that were minimal or lost at cellular scales. Specifically, FGF "solidifies" the dermal core, whereas BMP maintains fluidity and increases the mechanical activity of the margin. We hypothesized that the emergence of these two materially distinct, adjacent tissue phases produces an instability whereby the active, contractile fluid margin propels the inner solidified core into the epidermis to induce budding. Indeed, by coupling quantitative phase-field modeling and experimental data, we showed that these two phases create an unstable complex resolved through budding.

CONCLUSION: Our work shows that understanding the role of morphogens in morphogenesis requires characterizing emergent material and mechanical properties at the supracellular scale. This stands in contrast to the prevailing view that the functional effects of morphogens are on properties that can be characterized at the scale of individual cells, such as concentration sensing, proliferation, and chemotaxis. This paradigm highlights the need to distinguish between the proximal effects of morphogens, which include modulating gene expression of individual cells, and their ultimate functional effects, which enable the formation of distinct supracellular phases that are capable of morphological transformation. ■

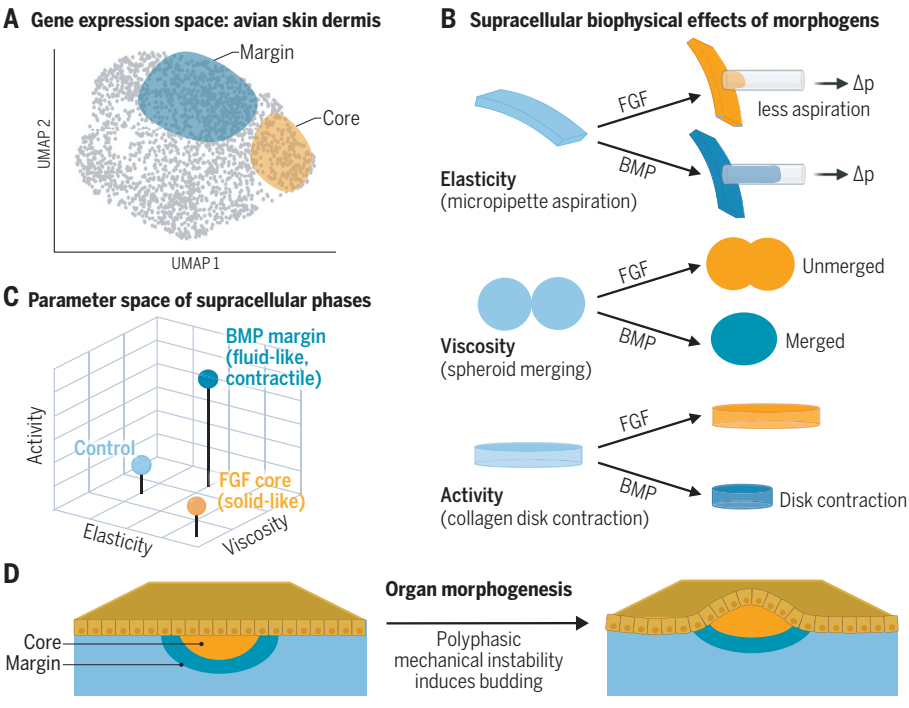

Morphogens enable interacting supracellular phases that shape organs. (**A**) Single-cell gene expression profiling of avian dermal cells uncovered two follicle domains (core and margin). UMAP, uniform manifold approximation and projection. (**B**) Morphogens tune supracellular material and mechanical properties. Δ*p*, change in pressure. (**C**) FGF enables a solid-like core, and BMP enables a contractile fluid-like margin. (**D**) A mechanical instability generated between domains with distinct material properties drives organ (skin) budding. [Created with BioRender.com]

The list of author affiliations is available in the full article online.
*Corresponding author. Email: ashyer@rockefeller.edu (A.E.S.); arodrigues@rockefeller.edu (A.R.R.)
†These authors contributed equally to this work.
‡These authors contributed equally to this work.
Cite this article as S. Yang *et al.*, *Science* **382**, eadg5579 (2023). DOI: 10.1126/science.adg5579

READ THE FULL ARTICLE AT
https://doi.org/10.1126/science.adg5579

Downloaded from https://www.science.org at Rockefeller University on July 10, 2024

RESEARCH ARTICLE

TISSUE MORPHOGENESIS

Morphogens enable interacting supracellular phases that generate organ architecture

Sichen Yang[1]†, Karl H. Palmquist[1]†, Levy Nathan[1], Charlotte R. Pfeifer[1], Paula J. Schultheiss[2,3], Anurag Sharma[4], Lance C. Kam[2,3], Pearson W. Miller[5], Amy E. Shyer[1]*‡, Alan R. Rodrigues[1]*‡

During vertebrate organogenesis, increases in morphological complexity are tightly coupled to morphogen expression. In this work, we studied how morphogens influence self-organizing processes at the collective or "supra"-cellular scale in avian skin. We made physical measurements across length scales, which revealed morphogen-enabled material property differences that were amplified at supracellular scales in comparison to cellular scales. At the supracellular scale, we found that fibroblast growth factor (FGF) promoted "solidification" of tissues, whereas bone morphogenetic protein (BMP) promoted fluidity and enhanced mechanical activity. Together, these effects created basement membrane–less compartments within mesenchymal tissue that were mechanically primed to drive avian skin tissue budding. Understanding this multiscale process requires the ability to distinguish between proximal effects of morphogens that occur at the cellular scale and their functional effects, which emerge at the supracellular scale.

Organ morphogenesis involves increases in morphological complexity, or symmetry breaking, through intrinsic processes of self-organization. Genetic and molecular investigation have identified conserved sets of proteins, termed morphogens, that have been shown to be essential for the creation of proper tissue morphology (*1*–*3*). Theoretical models and experimental studies have proposed that morphogens initiate morphological symmetry breaking through chemical diffusion mechanisms. Resulting spatial differences in morphogen concentration create molecular prepatterns that then instruct structural changes across a tissue (*4*–*7*). By contrast, an alternative source of symmetry breaking has been proposed by theoretical work focused on cell and tissue mechanics, whereby mechanical instabilities amid cellular collectives can also serve to initiate symmetry breaking in a structurally homogeneous tissue (*8*, *9*). Given the increasing appreciation that organogenesis is an irreducibly multiscale phenomenon (*10*), a present challenge is to clarify and unambiguously link the respective roles played by morphogens and collective cell mechanics.

[1]Laboratory of Morphogenesis, The Rockefeller University, New York, NY 10065, USA. [2]Department of Biomedical Engineering, Columbia University, New York, NY 10027, USA. [3]Department of Medicine, Columbia University, New York, NY 10032, USA. [4]Electron Microscopy Resource Center, The Rockefeller University, New York, NY 10065, USA. [5]Center for Computational Biology, Flatiron Institute, New York, NY 10010, USA.
*Corresponding author. Email: ashyer@rockefeller.edu (A.E.S.); arodrigues@rockefeller.edu (A.R.R.)
†These authors contributed equally to this work.
‡These authors contributed equally to this work.

The avian skin has served as a canonical example of how morphogen-mediated prepatterning, which is achieved through putative Turing-like reaction-diffusion mechanisms, instructs the creation of a repetitive morphological pattern (*11*). However, a prepatterning-based role for morphogen-induced symmetry breaking was put into question by observations that follicle gene expression activation occurs at the same time and not before the onset of morphological changes (*12*). Instead, the initiation of follicle aggregates has been shown to be a direct result of the mechanical self-organization of dermal cells. Furthermore, this collective cell self-organization also results in the activation of gene expression cascades within emerging follicles through a mechanotransductive signaling pathway, which dispenses with the need for a molecular diffusion-based mode of establishing gene expression patterns across a field of tissue (*12*). A reconstitution system in which primary dermal progenitors are cultured on a collagen substrate that mimics the in vivo environment has revealed that cell–extracellular matrix (ECM) networks are essential for collective cell self-organization. Moreover, theory coupled to experiment indicates that the cell-ECM composite creates effective material properties at the supracellular scale that are analogous to those of a contractile fluid. (*13*). The fluid nature of tissues was highlighted in a seminal work several decades ago (*14*). Together, these results emphasize the need to consider supracellular material properties necessary for tissue symmetry breaking that are not reducible to the properties of individual cells.

Although recent studies indicate that morphogens do not establish prepatterns to instruct morphological symmetry breaking in the avian skin, decades of study have shown that numerous established morphogens are essential for feather formation and are expressed in patterns that coincide with emerging follicles (*11*, *15*). Thus, the avian skin offers an ideal opportunity to go beyond canonical morphogen paradigms to uncover unappreciated roles for morphogens in shaping tissues. In this work, we set out to characterize the role of morphogens in avian skin during feather follicle morphogenesis and their relation to emergent supracellular mechanics.

Characterization of supracellular structural motifs that underlie follicle emergence

Given that it has been recently established that follicle-specific expression of genes emerges just after the follicle primordium initiates (*12*), we set out to perform a spatiotemporal analysis of supracellular structural changes that occur at and after this time stage. To do so, we visualized the nuclei, actin, basement membrane, and epidermal cell membranes in sections of dorsal (back) skin from embryonic day 6 (E6) to E8 chicken embryos. This characterization indicated that follicle emergence could be subtyped into three periods, which we term the precondensation, condensation, and budding stages. During the precondensation stage, the epidermis was a single-cell thick cuboidal epithelium (Fig. 1A). Whereas the epidermis retained this morphology, the basement membrane transitioned to a buckled architecture. At the condensation stage, the epidermal placode appeared as a thickened pseudostratified epithelium, and the basement membrane further buckled above an aggregating, actin-rich dermal condensation (Fig. 1A). The end of the condensation stage was marked by a dip of the epidermis and basement membrane into the dermis, which was associated with a reduction of basement membrane buckling. Notably, up to this time point, which included the precondensation and condensation stages, the surface of the skin tissue remained flat. After the establishment of the follicle primordia, as the follicle gene expression program was being initiated, the epidermis and basement membrane inverted from a downward to an upward curvature (Fig. 1A). After this inversion, the epidermis and dermis began to protrude or bud out of the plane of the back skin. During this budding stage, the laminin signal within the basement membrane at the center of the bud markedly decreased and appeared as puncta within the dermal follicle condensate (Fig. 1A).

Although follicle and interfollicle domains across the plane of the skin have been previously identified (*16*), our characterization of supracellular structure revealed a symmetry-breaking event that occurs within the dermal

Downloaded from https://www.science.org at Rockefeller University on July 10, 2024

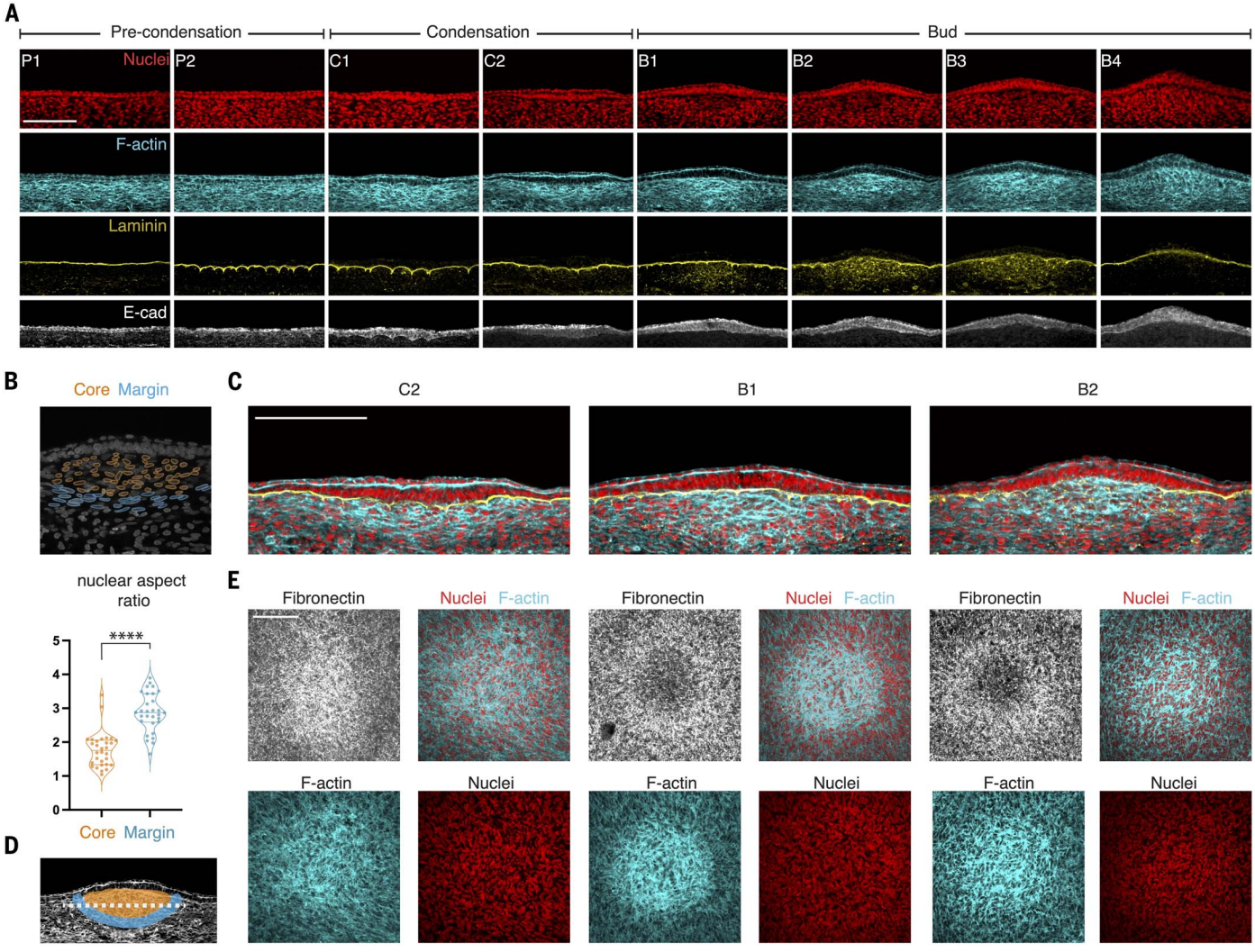

Fig. 1. The emergence of distinct structural domains in the dermis coincides with feather follicle primordia budding. (**A**) Developmental time course of fixed, longitudinal sections showing the transformation from naïve precondensate skin (P1 and P2) to the condensation of a multicellular aggregate in the dermis (C1 and C2) to the formation of a mature feather follicle primordium that protrudes from the two-dimensional surface of the skin (B1 to B4). Maximum intensity projections of F-actin (phalloidin), nuclei (DAPI), the basement membrane (laminin), and epithelial cell junctions (E-cadherin) are shown. (**B**) Overlay of example nuclear outlines in the core (orange) and margin (blue) (top) that correspond to the populations of nuclei used to calculate the aspect ratio (bottom). N = 30 nuclei per region. (**C**) Maximum intensity projection showing the composite of nuclei (red), actin (cyan), and laminin (yellow) at three stages from the corresponding longitudinal sections in (A). (**D**) Schematic showing the approximate z-section plane in (E). The dotted line indicates the approximate z-plane section for images in (E). (**E**) Maximum intensity projections of a single feather follicle primordium at three stages corresponding to (C) that are stained for fibronectin, F-actin, and nuclei in whole-mount skin samples. Scale bars are 100 μm. ****$p < 0.0001$.

condensate as the follicle buds. Specifically, two domains emerged within the condensate, which we term the core and the margin. These domains displayed differences in cytoskeletal, nuclear, and ECM arrangement. The core displayed increased actin, round and isotropically arranged nuclei (Fig. 1, B to D, and fig. S1A), and diminished fibronectin (Fig. 1E). By contrast, the margin contained elongated and aligned nuclei (Fig. 1, B and D, and fig. S1A), less actin, and increased fibronectin (Fig. 1E). Temporally, these domains emerged during the condensation stage and persisted through the budding stage, which suggests that a shift in the position of supracellular domains contributes to budding out of the plane.

Identification of distinct transcriptomic signatures for supracellular structural domains

After uncovering the existence of core and margin supracellular domains, we sought to determine whether each domain corresponded to a distinct gene expression program. We performed single-cell sequencing on the E8 chick back skin, a time point that includes a range of precondensation, condensation, and budding stages (Fig. 2A). Although the dermis at this stage was composed mainly of fibroblast progenitors, blood, muscle, and immune fates began to be found in the tissue as well (Fig. 2B). To focus on regional differences within dermal fibroblasts, we removed cells with clear nonfibroblast fate from our final analysis (fig. S2A). Using fluorescence in situ hybridization (FISH), we identified a large cluster within the fibroblast population as subjacent to the follicle-forming dermis (fig. S2B). We then focused our analysis on dermal fibroblasts of the superficial dermis, and clustering analysis revealed several distinct clusters (Fig. 2C and fig. S2, C and D). Notably, we found clusters expressing

Downloaded from https://www.science.org at Rockefeller University on July 10, 2024

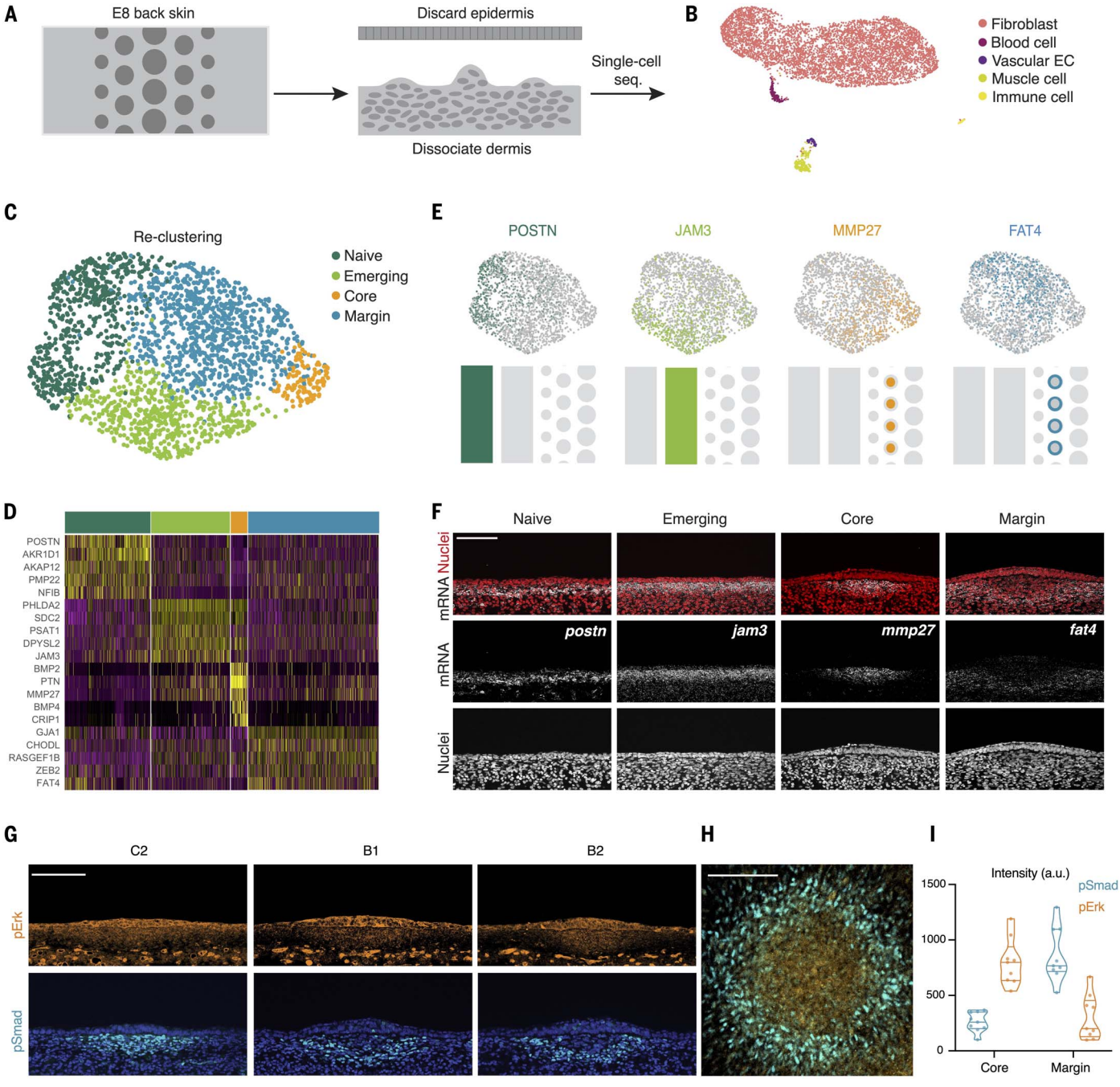

Fig. 2. Molecular characterization of the skin reveals spatiotemporally segregated dermal domains with distinct signaling activity. (**A**) Schematic of the single-cell mRNA sequencing experiment representing skin collection from the embryo and dermis isolation. (**B**) Uniform manifold approximation and projection (UMAP) visualization of the initial clustering analysis. Five cell types are identified: fibroblasts, blood cells, vascular endothelial cells (EC), muscle cells, and immune cells. (**C**) UMAP visualization of reclustering analysis after isolating cells of interest for follicle morphogenesis. Four dermal fibroblast populations are identified: naïve, emerging, core, and margin. (**D**) Heatmap showing selected differentially expressed genes for each cluster in (C). (**E**) Feature maps showing the gene expression profile for the marker genes of each cluster in (C), and schematics showing where they are expressed in vivo on the basis of FISH analysis. (**F**) FISH analysis of the marker genes for each cluster in (C). Maximum intensity projections of respective mRNA and nuclei (DAPI) are shown. (**G**) Immunofluorescent images showing the developmental time course of stages as the two domains emerge, stained for FGF-activity (pERK, orange) and BMP activity (pSMAD, cyan), and nuclei (blue). (**H**) Immunofluorescent images showing the maximum intensity projection of pSMAD and nuclei in whole-mount skin samples at stage B2. (**I**) Quantifications of normalized intensity for pSMAD and pERK in the core and margin regions from the B2 stage in (G). *N* = 3 embryos for both pSMAD and pERK, with three ROIs averaged for the core and margin per embryo. a.u., arbitrary units. Scale bars are 100 μm.

Downloaded from https://www.science.org at Rockefeller University on July 10, 2024

markers that correspond to the core and margin domains of the follicle dermis (Fig. 2, C to F). Two other clusters expressed markers associated with more nascent stages before follicle budding (Fig. 2, C to F). Thus, as suggested by our morphological characterization, the dermal condensate of the follicle is composed of two domains with differing gene expression. In addition, whereas many single-cell sequencing studies map differences between cell types across a tissue or through time, our analysis highlights that single-cell sequencing can also reveal finer distinctions within a single type (e.g., dermal progenitor). Focusing on a small yet morphologically important temporal window, we identified distinct clusters that, rather than marking divergent final cell fates, indicated the tuning of cell properties that enabled marked structural differences visible at the supracellular scale.

Fibroblast growth factor and bone morphogenetic protein signaling activity delineates distinct domains during follicle budding

We hypothesized that the core and margin domains within the budding follicle, which differed in their supracellular structural as well as their transcriptional profiles, depended on differential morphogen activity. Morphogen expression characterization in previous studies has focused on distinguishing between follicle and interfollicle expression during the condensation and budding stages (*17*, *18*). To discover morphogen candidates critical for mediating the core and margin domains, we focused on morphogens expressed at the onset of follicle formation and morphogens that appeared in our single-cell dataset (*15*, *19*, *20*). The intersection of these criteria revealed fibroblast growth factor (FGF) and bone morphogenetic protein (BMP) as the two leading candidates for further analysis. FGF and BMP ligands are expressed in the epidermis and core dermis (fig. S3A) (*21*, *22*); however, we used antibody staining of phosphorylated SMAD (pSMAD) and phosphorylated extracellular signal-regulated kinase (pERK) to determine regional pathway activity.

With regard to FGF signaling activity, we found that the pERK signal coincided specifically with the core region of the follicle dermis but not the margin (Fig. 2, G to I). However, pSMAD transitioned from being localized to the condensate to coinciding with the margin at budding stages. Thus, at budding stages, BMP signaling activity did not overlap with its domain of gene expression (Fig. 2, G to I, and fig. S3A). We investigated the origins of this activity pattern and confirmed that the BMP inhibitor follistatin was expressed in the follicle epidermis (fig. S3, B and C) (*23*). The absence of pSMAD in the core indicates that follistatin inhibited BMP-pathway activity in the region in which BMP was expressed. Thus, this system of molecular activators and an inhibitor generates a margin that is exposed to BMP ligand that spreads from the secreting core but escapes the influence of follistatin, its pathway inhibitor. Both of these activity patterns appeared in discrete domains and were not present in a graded morphogen-type pattern, as might have been expected. Thus, FGF and BMP are the morphogens that are responsible for enabling the generation of distinct, neighboring domains before follicle budding.

Direct biophysical measurements reveal emergent elasticity changes at the supracellular scale

To complement our molecular characterization of the core and margin regions with biophysical characterization, we investigated the material properties in these domains by applying atomic force microscopy (AFM) to frozen sections of the skin (Fig. 3A). We performed measurements using two probe sizes that differed by an order of magnitude (5 and 45 μm). Probe sizes of 5 μm or less are frequently used to measure cellular- and subcellular-scale stiffness (*24*). Our inclusion of a less commonly used large probe size allowed for the capture of properties at the supracellular scale. We found that at the supracellular scale (45-μm probe), the core of the tissue was 2.38-fold stiffer than the margin (Fig. 3B). This fold difference in stiffness between the core and margin decreased to 1.48-fold when stiffness was measured at the cellular scale (5 μm). This dependence of the core-margin stiffness differential on the length scale of measurement indicates that the supracellular scale can possess emergent material properties that are not detectable at the cellular-length scale. Such length-scale dependence of material properties is analogous to observations made in granular media (e.g., sand) (*25*).

Given the spatial correlation between morphogen activity (core-FGF, margin-BMP) and supracellular material property differences (core, more stiff; margin, less stiff), we tested a model whereby morphogens, through the tuning of many cell features, enable emergent tissue material properties of adjacent domains. Morphogens are often characterized as serving a role in inducing a new cell fate (e.g., in directed differentiation protocols) (*26*, *27*). Furthermore, when considering effects on morphology, studies have centered around individual cell behaviors, in particular, growth and migration (*7*, *18*, *28*, *29*). In this work, however, we sought to determine whether the ultimate functional effect of morphogens arises on a length scale beyond the detection of a single cell. This line of inquiry is supported by an increasing appreciation for how biophysical features of cellular collectives influence morphogenesis (*30*–*32*).

To test whether FGF and BMP were sufficient to affect stiffness at the supracellular scale, we performed AFM on ex vivo dermal reconstitutions treated with either FGF or BMP and compared the results with those from control samples. Treatment with morphogens lead to a significantly larger change in material properties (stiffness) detected at the supracellular scale (45-μm probe) than at the cellular scale (Fig. 3C). To confirm these findings using an alternative yet established tool that directly measures material properties, we performed micropipette aspiration (MPA) (Fig. 3D) on dermal reconstitutions treated with either FGF or BMP and compared the results with those from control samples (*33*). To perform cellular- and supracellular-scale analyses, samples were aspirated using pipette tips of 5 to 7 μm and 50 μm, respectively. We found significant differences in stiffness in morphogen-treated samples when measurements were made at the supracellular scale (50-μm probe) but no significant differences between treatment and control samples when measurements were made at the cellular scale (5-μm probe); this absence of significant differences at the cellular scale further corroborates the emergent nature of these morphogen-enabled effects.

Finally, we developed a method of inferring material phase property changes at the supracellular scale based on scanning electron microscopy (SEM). We noted that the process of drying during preparation for SEM imaging generated a pattern of cracks across dermal reconstitution samples. These crack patterns differed across treatment conditions, with substantially larger fractures observed in FGF-treated samples than in BMP-treated and control samples (fig. S4A). We reasoned that these patterns of fractures may be akin to the cracks that form in many common materials upon drying, including sand and concrete. In these cases, the material shrinks as it dries to form predictable patterns of cracking, which are indicative of the physical properties of the material (*34*). Along these lines, we reasoned that the larger cracks that occurred with FGF treatment were indicative of increased brittleness or solidity. In addition, the absence of large- or medium-size fractures in BMP-treated samples indicated that they are the least brittle or solid-like. Given that the cracking pattern occurs at a scale greater than the cell, this assay offered a newly discovered opportunity to assess supracellular brittleness or solidity.

Taken together, these findings indicate that the ultimate functional effect of FGF and BMP is to enable material property changes that are emergent and therefore only detectible through measurements at the supracellular scale. These effects on material properties are exerted in tissue space, which suggests a functional role for morphogens in enabling the formation of physically distinct basement membrane–less

Downloaded from https://www.science.org at Rockefeller University on July 10, 2024

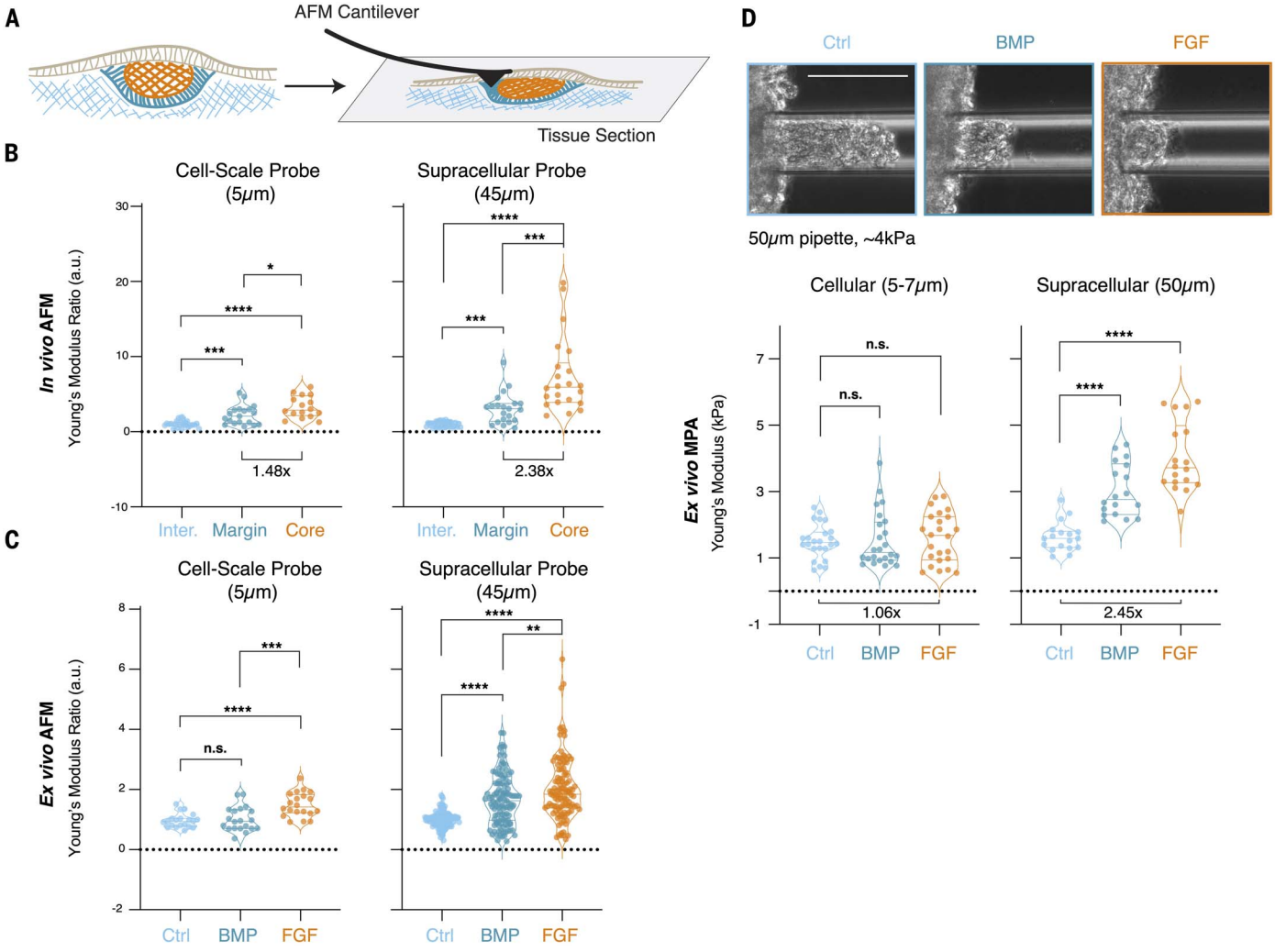

Fig. 3. Biophysical measurements reveal emergent elasticity changes at the supracellular scale. (**A**) Schematic of experimental approach for AFM analysis of in vivo tissue sections. (**B**) Results from in vivo AFM using cellular-scale (5 μm) and supracellular-scale (45 μm) probes. The ratio of Young's modulus with respect to the interbud (Inter.) value is plotted at both length scales. (**C**) Results from in vitro AFM using 5- and 45-μm probes on dense dermal reconstitutions treated with either BMP or FGF or left untreated (control). The Young's modulus ratio is plotted with respect to control values. (**D**) (Top) Example bright-field microscopy images of dense dermal reconstitutions being aspirated into a 50-μm glass pipette at maximum extension for control, BMP-treated, and FGF-treated samples. (Bottom) Young's modulus of dense dermal reconstitutions for control, BMP, and FGF conditions using two different pipette sizes: cellular (5 to 7 μm) and supracellular (50 μm). *N* = 16 to 32 measurements for six or seven follicles in (B), 20 measurements (each measurement is the average of a stiffness map containing a grid of measurements; see Materials and methods) over four independent cultures using the 5-μm probe and 113 to 120 measurements over four independent cultures using the 45-μm probe in (C), and 18 to 32 measurements over three independent trials in (D). Scale bar is 100 μm. **p* < 0.05; ***p* < 0.005; ****p* < 0.001; *****p* < 0.0001; n.s., not significant.

compartments that coexist and interact within a single mesenchymal tissue.

Integrating experiment and mathematical modeling reveals the effects of morphogens on supracellular viscous properties

Our direct measurements of stiffness by AFM and MPA indicated the presence of emergent material properties that relate to elastic or solid-phase properties. Given that tissues also concurrently possess viscous or fluid-like properties, we next sought to characterize viscous properties enabled by morphogens.

To do so, we developed an assay that shares conceptual resonance with those used to study molecular condensates (*35*). Specifically, the size and number of aggregates formed in suspensions of molecules enable the inference of material properties across the liquid-to-solid phase continuum (*36*). A greater number of smaller aggregates would indicate solid-phase properties, whereas a smaller number of larger aggregates would indicate fluid-phase properties. To adapt such assays to the supracellular scale, we cultured a low-density cell suspension of primary dermal cells as a hanging drop and then characterized patterns of cell condensation. Suspensions treated with no signal or BMP formed a few large spheroids (Fig. 4, A and B, and fig. S5B). Conversely, suspensions treated with FGF resolved into many smaller spheroids. These results suggest that cells exposed to FGF signaling generate supracellular material properties that are more solid-like than those of control and BMP-treated cells.

To further investigate viscous properties, we examined the ability of preformed spheroids to merge when placed in close contact. Fluid tissues will readily merge, whereas more–solid-like tissue will fail to merge (*37*–*39*). Indeed, FGF-treated spheroids failed to merge, whereas

Downloaded from https://www.science.org at Rockefeller University on July 10, 2024

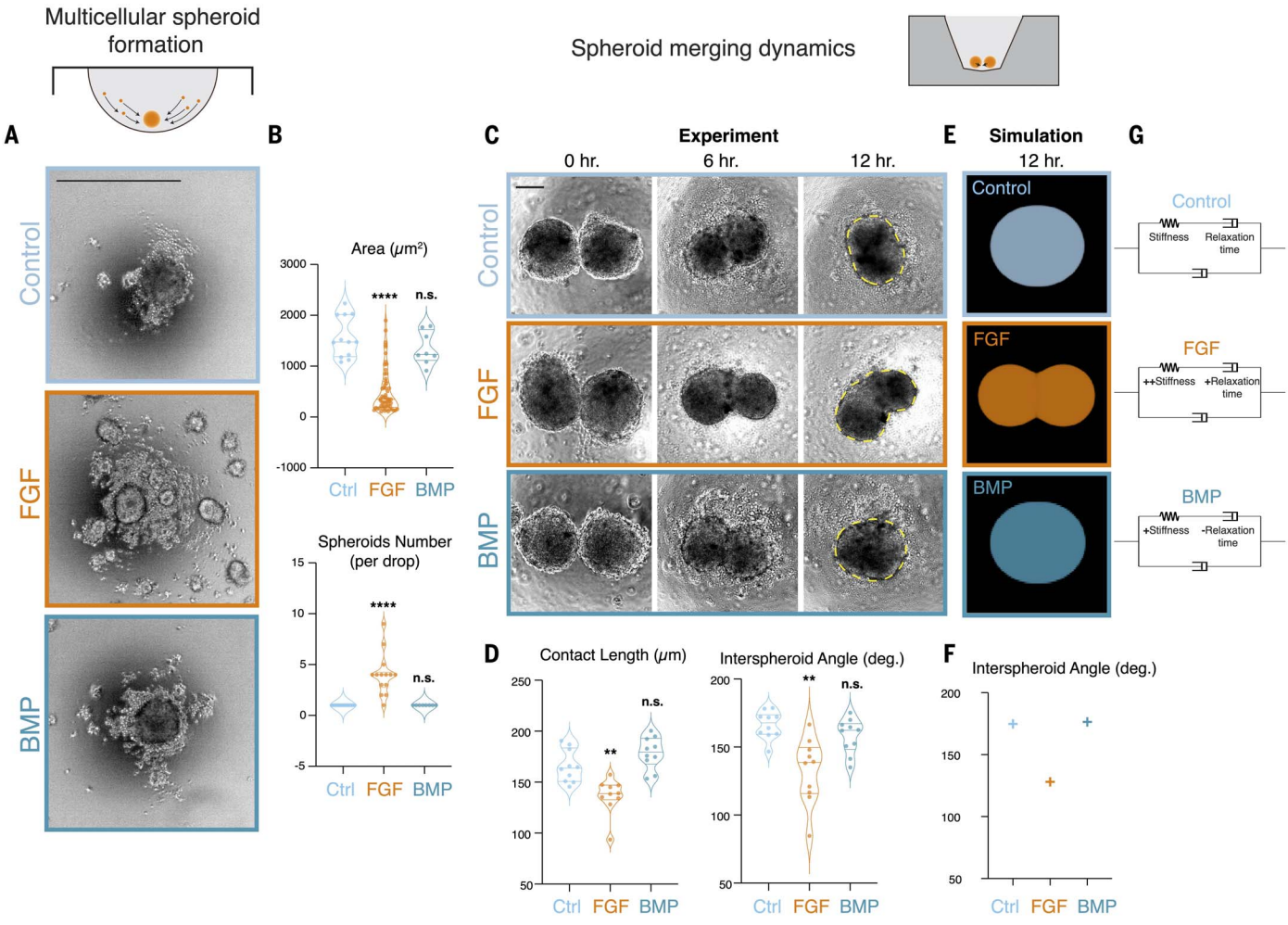

Fig. 4. Morphogens enable distinct viscous properties at the supracellular length scale. (**A**) Spheroids formed in a hanging drop of low–cell concentration suspensions. (**B**) (Top) Area of spheroids formed in (A). (Bottom) Number of spheroids per drop formed in (A). *N* = 8 to 12 drops per condition. (**C**) Merging dynamics of two spheroids initially formed in high–cell concentration suspensions for control, FGF, and BMP conditions. (**D**) Contact length and interspheroid angle (in degrees) for conditions shown in (C) measured at the 12-hour time point. *N* = 10 sets of spheroids per condition. (**E**) Simulations of droplet merger informed by AFM and MPA were used to deduce viscous relaxation timescales. Full details of these simulations are described in the supplementary text. (**F**) Interspheroid angle (in degrees) for conditions shown in (E) measured at the 12-hour time point. (**G**) Spring-and-dashpot model. Our experiments led us to characterize the dermal condensate as a viscoelastic fluid whose passive mechanical response can be represented by spring-and-dashpot diagrams. We observed changes in the mechanical response in response to morphogen treatment, with FGF condensates demonstrating increases in both the elastic modulus and the viscous relaxation timescale. BMP spheroids have increased stiffness but demonstrate a faster viscous relaxation consistent with increased fluidity. Scale bars are 100 μm. $^{**}p < 0.005$; $^{****}p < 0.0001$; n.s., not significant.

control and BMP-treated spheroids merged readily, further supporting the emergence of solid properties of an FGF-influenced cell collective (Fig. 4, C and D, and fig. S5A). We observed hallmarks of stiffness reflected in cytoskeletal architecture upon treatment with FGF that likely reflected cells in a stiffer environment (*40*–*43*) and also contributed to tissue stiffness (fig. S5C).

To gain a quantitative understanding of supracellular viscous properties, we developed a model to simulate spheroid merging (Fig. 4, E and F). By inputting values of stiffness and surface tension gained from MPA measurements, we were able to generate an estimate of the relaxation times of tissues under control and morphogen treatment conditions. Combined with our AFM and MPA measurements, these results provide a full characterization of the bulk material properties of this viscoelastic supracellular system. These material property estimates can be efficiently summarized in a spring-and-dashpot model that captures the viscoelastic supracellular responses that are made possible by morphogen activity (Fig. 4G). Specifically, FGF-exposed tissue has heightened elasticity as well as higher viscosity (relaxation time) than control tissue. Conversely, BMP-exposed tissue has moderate elasticity but reduced viscosity (relaxation time) compared with control tissue, which is consistent with our cracking assay results. Taken together, these results suggest that BMP-exposed tissues possess greater fluidity than control tissues, whereas FGF-exposed tissues possess greater solidity.

Morphogens tune supracellular activity by enabling changes in ECM architecture and traction forces

In addition to changes in viscoelastic properties, it is also possible for a supracellular material to modulate the extent of its "activity," which could serve as a key impulse for morphological transformation. To investigate this, we took advantage of our recently developed supracellular behavioral assay, which serves as a fluidity assay that assesses activity (*13*). In

Downloaded from https://www.science.org at Rockefeller University on July 10, 2024

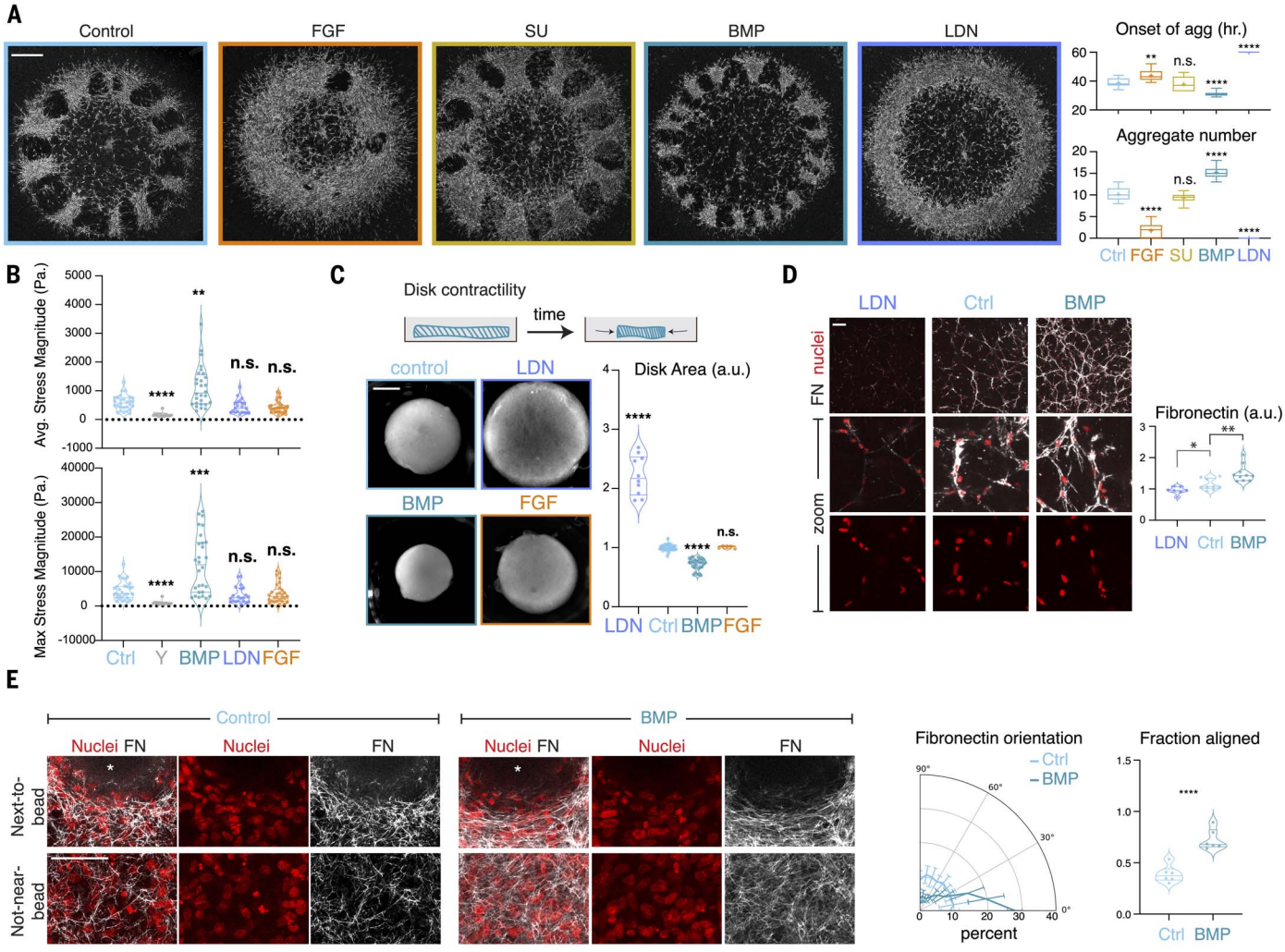

Fig. 5. Morphogens tune ECM architecture and traction force to generate supracellular contractility. (**A**) (Left) Bright-field microscopy images from the ring assay at the 48-hour time point after treatment with BMP, LDN, FGF, or SU5402 (SU), an FGF inhibitor. (Right) Onset of aggregation and aggregate number. N = 11 to 28 rings per condition. (**B**) Average and maximum traction forces for individual cells plated on polyacrylamide gels. N = 15 to 29 cells per condition. (**C**) (Left) Bright-field microscopy images of disk contraction (50 hours) (left) and disk area normalized to control area (right). N = 10 to 32 disks per condition. (**D**) Immunofluorescent images of nuclei and fibronectin in disks (left) and fibronectin intensity normalized to DAPI (right). N = 7 to 10 disk regions per condition. (**E**) (Left) Immunofluorescent images of dense dermal reconstitutions showing nuclei and fibronectin (FN) surrounding uncoated agarose beads (asterisk). (Right) Fibronectin orientation (0° is tangent to bead surface) and the fraction of fibronectin aligned around a bead. N = 3 reconstitutions per condition (one to three regions each). a.u., arbitrary units. Scale bars are 500 μm in (A), 2 mm in (C), 50 μm in (D), or 100 μm in (E). *p < 0.05; **p < 0.005; ****p < 0.0001; n.s., not significant.

this assay, skin fibroblasts form a supracellular contractile fluid that resolves into a pattern of aggregates. In line with our measurements of stiffness and relaxation time, the addition of FGF to the behavioral assay interfered with aggregate formation (Fig. 5A and movie S1), which suggests a transition to a less active, solid material. By contrast, treatment with BMP increased the speed of aggregate formation as well as the number of final aggregates (Fig. 5A and movie S1), which prior theoretical modeling suggested would be the result of a more actively contractile fluid (*13*). Taking these results together with our observations of in vivo architecture, we hypothesized that the key functional output of FGF- and BMP-pathway activity is to create a solid core surrounded by a contractile fluid margin.

Our multicellular behavioral assay revealed a difference between BMP-treated and control cells that indicates enhanced activity mediated by contractility (Fig. 5A and movie S1). Thus, we investigated whether BMP serves to increase contractility by using traction force microscopy (TFM). Freshly harvested dermal progenitors were cultured atop a polyacrylamide hydrogel at a low density such that individual cells exerted traction in isolation. Embedded green fluorescent protein (GFP) beads within the hydrogel enabled the tracking and measurement of gel displacement. When cultures were treated with FGF, traction forces remained similar to those in control cultures. However, BMP treatment increased traction forces exerted by dermal cells as compared with control cells. BMP inhibition with LDN-193189 (LDN) compound did not have a significant effect on individual cell contractility (Fig. 5B).

We next sought to determine how individual cell changes in traction that are enabled by BMP manifest at the supracellular scale. We aimed to generate a context that mimicked the planar geometry of the bud margin, where BMP is active, rather than the spherical shape relevant to the core (Fig. 5C). To this end, we cultured cells in freed collagen disks and measured disk retraction, comparing areas across conditions (Fig. 5C). In line with our hypothesis,

Downloaded from https://www.science.org at Rockefeller University on July 10, 2024

BMP-treated disks contracted more than control disks and LDN-treated disks contracted less than control disks (Fig. 5C). The fact that LDN treatment did not have a significant effect on the traction forces of individual cells in isolation but did affect supracellular disk contraction indicates the presence of activity-related processes that only appear at the supracellular scale.

Next, we investigated which cellular features are tuned by BMP to generate increases in supracellular contractility. Motivated by our observation that the BMP-pSMAD active margin shows stronger fibronectin staining (Fig. 1E), we considered that the increase in collagen disk contraction could be due to a more interconnected ECM network (*44*, *45*). In agreement with our in vivo observations, BMP-treated collagen-disk cultures displayed more fibronectin deposition than control cultures (Fig. 5D). Conversely, when disks were treated with LDN, fibronectin deposition was nearly absent (Fig. 5D). These results support a role for fibronectin downstream of BMP in enhancing collective contraction in the fluid-like margin.

With an understanding of the two distinct tissue material properties generated by FGF and BMP morphogens, we explored the possibility that the emerging solid core and contractile fluid margin may mutually enhance each other's material properties. Cells in the BMP-active margin displayed increased elongation and alignment (Fig. 1), but we did not observe similar levels of alignment or elongation in dense dermal reconstitutions treated with BMP (Fig. 5E and fig. S6, A and B). Noting that, in vivo, the margin cells align around a more-solid core, we hypothesized that BMP-enabled alignment may only occur in the presence of a neighboring solid tissue. To test this hypothesis, we incorporated agarose beads into dense dermal cultures to mimic the round solid core. Indeed, BMP-treated cells displayed more alignment around the bead than control cells (Fig. 5E and fig. S6A). Thus, the material properties of the FGF-active core provide a solid substrate for the surrounding contractile fluid layer of the margin to orient around, and the core serves as a force guide that orients margin contractility. When considering a mutually conditioning interaction, we reasoned that the oriented contraction of the margin likely compresses the core to further solidify it. Indeed, cytoskeletal elements, including vimentin, are up-regulated in compressed fibroblasts to protect the nucleus and induce a form of strain stiffening (*43*). Thus, each phase may be essential in amplifying the properties of the other, further separating the phase domains.

Interactions between phases generate stresses that break morphological symmetry

Next, we investigated the morphological consequences of these interacting tissue phases. We hypothesized that a fluid margin contracting around a solid core could generate forces in the dermis sufficient to propel the follicle out of the plane of the skin. Such a mechanism is distinct from those based on cell migration by means of chemotaxis or differential growth through proliferation, which focus on individual cell behavior rather than emergent supracellular properties. In line with our hypothesis, we saw an effect on budding when tuning stiffness and contractility. Specifically, using a skin explant culture in which the process of budding occurs ex vivo, we stiffened skin explants through the addition of genipin, a crosslinking agent, which decreased or blocked budding when low or high concentrations were added, respectively (Fig. 6A) (*46*). Conversely, when contractility is decreased in explants, which would predominantly affect the contractile margin, budding is inhibited (*12*).

Budding requires transformation of the overlying epidermis. We thus investigated the role of the epidermis in this process. To do so, we excised tissue at successive follicle stages and performed live-tissue dissections during which we removed the epidermis. Immediately after removal, we fixed the tissue and then characterized the resulting architecture in tissue sections. At the condensation stages, when the two tissue phases had yet to form, the dermal tissue remained in plane. However, after establishing the margin and core domains, the follicle dermis protruded upon epidermal removal (Fig. 6B). These results suggest that interactions between the core and margin tissue phases generate residual stress that has the mechanical potential to propel the bud out of the plane. Furthermore, these results show that the physical presence of the epidermis initially resists this action.

How, then, does the core-margin complex act to propel the bud given the presence of the overlying epidermis? Guided by our observations that the intensity of laminin in the basement membrane decreased as the particulate staining in the subjacent dermis increased (as shown in Fig. 1A), we investigated whether digestion of the basement membrane is a critical step that permits the forces in the dermis to generate a bud. In line with this model, our single-cell mRNA sequencing results revealed a number of matrix metalloproteinase (MMP) genes expressed specifically in the core of budding follicles (as shown in Fig. 2F). To test the idea that an MMP-based digestion of the basement membrane is essential for multiphase sculpting of the tissue, we inhibited MMP activity in explant culture. Indeed, the basement membrane in the MMP inhibitor condition remained intact and continued to buckle rather than flatten (Fig. 6C). Furthermore, when we inhibited MMP activity, the bud failed to protrude (Fig. 6C). These results demonstrate that in addition to the forces generated in the dermis through the interactions of the core and margin domains, the weakening of the basement membrane is a critical event that is required for the follicle to protrude through the plane of the skin.

With an understanding of the properties of the components and their putative interactions, we set out to build a quantitative physical model that could predict the organ-level consequences of the interacting domains in the skin to recapitulate this process. We chose a phase-field formalism because it allows for explicit representation of multiple material phases and easily interpretable governing equations. Furthermore, it is well suited for incorporating the distinct active properties of the material phases. Limiting the model to two dimensions, we describe this process as a free-boundary problem, in which different phases can deform and exert forces on one another but have a minimum tendency to mix with one another (Fig. 6D and movie S2). The model allowed for local manipulation of viscoelasticity, geometry, and activity of each material phase as well as global manipulation across all phases (see the supplementary text). Notably, the model is constructed so that all of the bulk material properties of each phase can be estimated or directly measured from our experiments.

First, we validated that the physical model could recapitulate the morphodynamics of wild-type follicle budding based on experimentally derived parameters for phase geometry, relative values of interfacial energies, and bulk mechanical properties (Fig. 6D). To test the generalizability of the model, we performed in silico perturbations that mimic the experimental manipulations described above. Indeed, our model predicts that increasing the stiffness and decreasing the contractility of the dermis prevents budding in a dosage-dependent manner (Fig. 6E, fig. S7A, and movies S3 and S4). Furthermore, the removal of the epidermal layer in the model predicts the dermal protrusion observed in our epidermal removal experiments (Fig. 6F, fig. S7B, and movie S6). Next, we tested whether the model recapitulates the finding that basement membrane digestion is needed for budding. To do so, we excluded weakening the epidermis from the model, and, indeed, the model predicted that the skin would fail to bud without this event (Fig. 6G, fig. S7A, and movie S5).

Our model also provided an opportunity to test how modulating multiphase tissue properties could account for variance in follicle budding across the body. To test our theory in cases other than the back skin bud, we took advantage of the varying bud geometries observed across the body. When comparing the geometry of follicles in the skin of the back to that of the follicles in the skin of the head, we found that the profile of the head bud is more extended and prominent (Fig. 6, H and I,

Downloaded from https://www.science.org at Rockefeller University on July 10, 2024

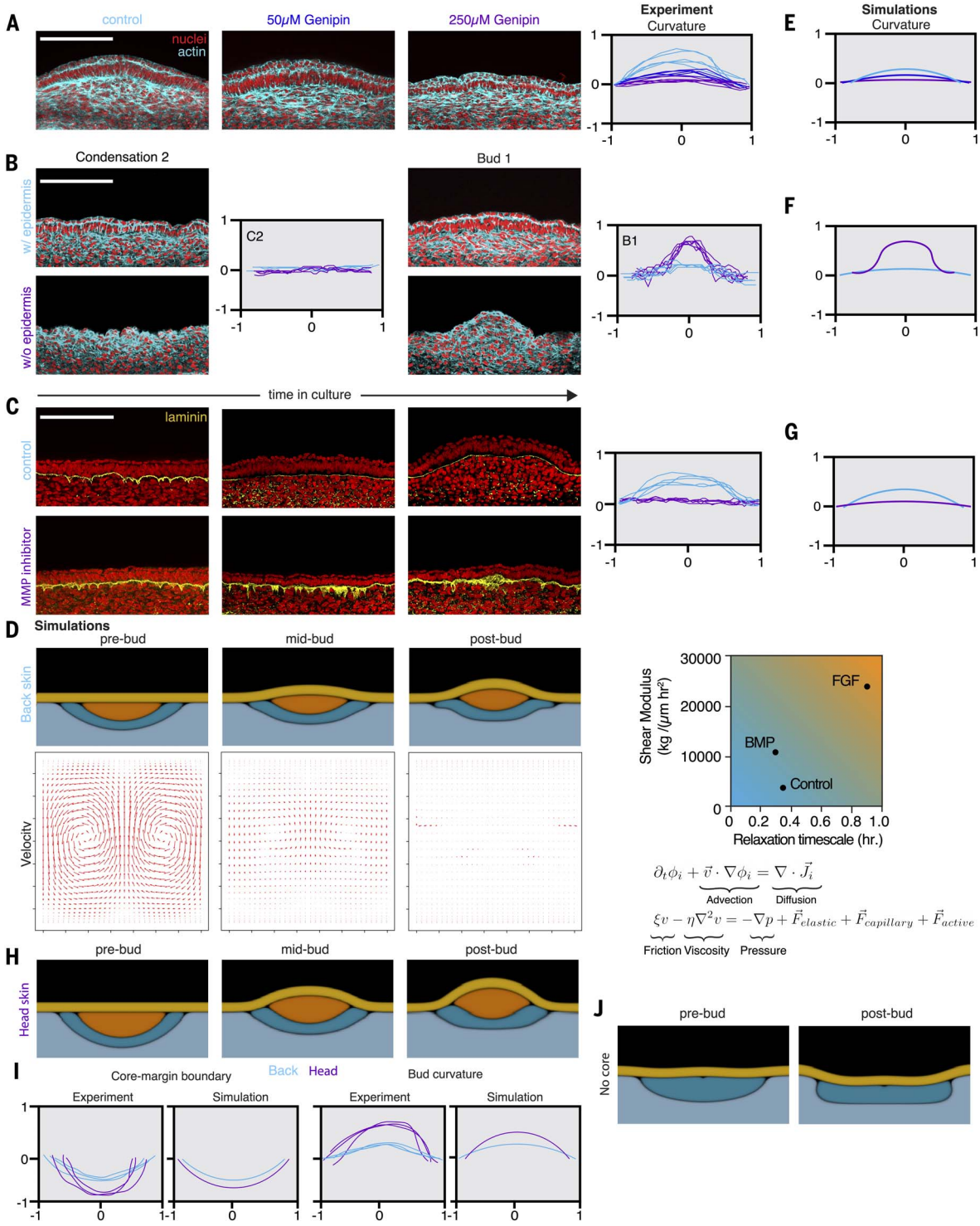

Fig. 6. Interactions between domains with distinct material properties underlie budding. (**A**) Longitudinal sections of control and genipin-treated (stiffened) explants stained for nuclei (red) and F-actin (cyan) (left) and curvature profiles (right). *N* = 5 or 6 follicles per condition. (**B**) Sections stained for nuclei (red) and F-actin (cyan) (left) and curvature profiles (right) from epidermis-removal experiments analyzed before (condensation 2) and after (bud 1) the core and margin domains emerge. *N* = 5 or 6 follicles per condition. (**C**) Sections (left) and curvature profiles (right) of control explants and those treated with MMP inhibitor (marimastat) stained for nuclei (red) and Laminin (yellow). The curvature profile shown is that for the final time point (48 hours). *N* = 5 follicles per condition. (**D**) (Left) Phase-field model simulations showing the budding process; the contractile active fluid margin is shown in dark blue, and the viscoelastic solid core is shown in orange (top). Anisotropic contractility generates a rotational flow that produces upward motion of the follicle (bottom). (Right) Parameter space plot showing the relative relaxation timescale and elasticity of samples treated with either BMP or FGF or left untreated (control) (top). A summary of the mathematical model, which treats the tissue and surrounding medium as a layered collection of distinct material phases (bottom). Extratissue fluid (black) is modeled as a passive viscous fluid, whereas tissue layers are treated according to the viscoelastic model described in the supplementary text.

Downloaded from https://www.science.org at Rockefeller University on July 10, 2024

Deformation of the tissue is driven by an anisotropic contractility in the condensate margin region (dark blue). The core region (orange) and epidermis have strain relaxation timescales on the order of or exceeding biological timescales, whereas the rest of the dermis relaxes an order of magnitude faster. (**E** to **G**) Simulation curvature profiles corresponding to (A) to (C), respectively, where stiffness is tuned (E), the epidermis is removed at 1 hour (F), or the epidermis is not weakened in order to model the MMP inhibitor experiments (G). (**H**) Phase-field simulations modeling domain geometry in the head. (**I**) Profiles of the core-margin boundary (prebud) and bud shape (postbud) for the back (cyan) and head (purple) from both experiment and simulation. $N = 3$ follicles per condition. (**J**) Phase-field simulations for tissue that lacks the core domain at the prebud- and postbud-equivalent stages. For details on simulation perturbations, see the supplementary text. Scale bars are 100 μm.

fig. S7C, and movie S7). In considering what might cause this shape in our physical model, we found that a critical parameter is the geometry of the domains, with a deeper margin leading to an in silico prediction that resembles the head bud profile. Indeed, we observed that the pSMAD region encircles a larger core domain (Fig. 6I, and fig. S7C). Further, the geometry of the more protrusive bud and the increased follicle spacing in the head are consistent with what has been observed previously in cases of increased contractility (*12*). Inputting the domain geometry together with increased contractility leads to a budding profile that mimics the head-follicle bud shape (Fig. 6, H and I, and fig. S7C). Interestingly, in the absence of force guidance provided by the solid core domain, it becomes possible for our model to achieve a concave rather than convex outcome (Fig. 6J, fig. S7D, and movie S8), which mimics invagination after aggregation seen in structures like hair follicles (*47*). This suggests that these multiphase interactions may be generalized beyond budding to break the tissue plane, either inward or outward.

Discussion

Given that tissue symmetry breaking is a multiscale, self-organizing process, it is a challenge to identify the functionally salient mechanical events that lead to increases in morphological complexity. Rather than focus on the behavior of individual cells, our experimental identification of emergent supracellular material properties led us to focus on the mechanics that arise between two distinct supracellular material phases. Our study shows that phase differences in tissues can arise not only in time as a tissue matures (*31*, *48*, *49*) but also concurrently in space to create a tissue-scale mechanical instability.

We show that morphogens are responsible for enabling these separated phases. By linking phase concepts to supracellular mechanics, we reveal a role for morphogens in creating a morphological order that is distinct from canonically proposed roles. Canonical accounts of the role of morphogens focus on effects—including morphogen concentration sensing, proliferation, and directed migration or chemotaxis—that can be characterized at the scale of a single cell (*7*, *18*, *28*, *29*). By contrast, our results support a model in which the effect of morphogens on emergent material properties at the supracellular scale must be considered. Through such consideration, we find that morphogens enable the creation of basement membrane–less tissue compartments within a mesenchymal tissue.

The creation of distinct phases at the subcellular scale to serve as membraneless compartments has been broadly noted (*35*) but also questioned with regard to functional relevance (*50*). In this work, we show that a clear functional role for compartments at the supracellular scale is to generate polyphasic complexes that, through their geometric arrangement, are mechanically primed to increase ordered morphological complexity.

Our findings indicate that it is necessary to distinguish between the proximal effects of morphogens, which include modulating gene expression within individual cells, and their ultimate functional effects, which enable the formation of distinct supracellular phases. Our study supports a model in which the subtle tuning of hundreds of genes at the individual-cell scale can coalesce into emergent and discrete material and mechanical properties that contribute to the creation of organ morphologies.

We hypothesize that morphogen-enabled polyphasic supracellular juxtaposition may generate tissue architecture in other organs. In addition, such processes may be present in pathological contexts such as tumors, in which cancer associated fibroblasts may tune their material properties and subsequent supracellular mechanical behavior in response to chemical signals in order to potentiate aberrant morphogenesis.

Materials and methods

Embryos and dissections

Embryonic back skins, consisting of one to five rows of follicles, were dissected, and the epidermis and dermis were separated by peeling apart the two layers after 15 min in cold calcium- and magnesium-free Hanks' balanced salt solution (HBSS). Extracted dermises from several embryos were combined and dissociated in a mixture of trypsin and collagenase at 37°C for 10 min. Acellular tissue components were removed in a 40-μm filter.

Fertilized chicken eggs (white leghorn) were obtained from commercial sources, incubated at 37.8°C, and staged according to Hamburger and Hamilton (*51*).

Cell and tissue culture assays

Collagen disk assays

Dissociated dermal cells from E7.5 back skins consisting of one to three rows of emerging follicles were diluted in full media [10% fetal bovine serum (FBS), 2% chick serum (CS)] to 5000 cells/μl. Collagen-I solution at 3 mg/ml was prepared from a 5-mg/ml collagen-I stock (Ibidi, no. 50201) by mixing collagen at 0.6X total volume, NaOH at 0.0201X total volume for neutralization (for a pH of roughly 7.35), and full media. Cells and collagen-I solution were then mixed 1:1 to form a final cellular concentration of 2500 cells/μl in 1.5-mg/ml collagen solution. Disks were prepared by adding 200 μl of the resulting collagen-cell mixture into a non–tissue culture–treated 48-well plastic bottomed plate and polymerized for 1 hour at 37°C. Disks were released from the bottom of the plate by moving a small pipette tip around the polymerized disk. Full media, FGF (R&D, 273-F9, 400 ng/ml), BMP (R&D, 5020-BP, 100 ng/ml), or LDN (TOCRIS, no. 6053, 100 nM) was added to the disks. Disks were cultured at 37°C with 5% CO_2 in a humid environment and subsequently imaged manually.

High–cell concentration suspensions for spheroid formation and merging

Dissociated dermal cells from E8 back skins consisting of three to five rows of emerging follicles were diluted in full media to 3000 cells/μl. Spheroids were generated by culturing cells in 5-μl drops upside-down in a 100-mm–by–20-mm tissue culture plate at 37°C with 5% CO_2 in a humid environment for 48 hours. Full media, FGF (400 ng/ml), or BMP (100 ng/ml) was added before plating the 5-μl drops for culturing of treated spheroids. Resulting spheroids were added into 200 μl of full media with a pipette into a 96-well Corning spheroid microplate (CLS4515). Spheroid merging was visualized in a BioTek Biospa 8 at 37°C with 5% CO_2 in a humid environment (~93% humidity) and were automatically transferred for imaging every hour.

Low cell concentration suspensions for spheroid formation

Dissociated dermal cells from E8 back skins consisting of three to five rows of emerging follicles were diluted in full media to 1300 cells/μl. Cells were cultured in 17-μl drops upside-down in a 100-mm–by–20-mm tissue culture–treated plate for 48 hours. Full media, FGF (400 ng/ml), or BMP (100 ng/ml) was added before plating the 17-μl drops for culturing of treated hanging drop cultures. Spheroids were cultured at 37°C with 5% CO_2 in a humid environment and subsequently imaged manually.

Downloaded from https://www.science.org at Rockefeller University on July 10, 2024

Ex vivo ring assay

Dissociated dermal cells from E8 back skins consisting of three to five rows of emerging follicles were diluted to 2100 cell/μl in full media, plated on collagen-I that was stored overnight at 4°C, and incubated before plating for 30 min at 37°C in a drying incubator, as previously reported (*13*). Cells were incubated at 37°C for 1 hour, and then full media, FGF (200 ng/ml), SU5402 (TOCRIS, no. 3300, 10 μM), BMP (100 ng/ml), or LDN (1 μM) was added to the well. For all long-term imaging experiments, cells plated on collagen-I were incubated in a BioTek BioSpa 8 at 37°C with 5% CO_2 in a humid environment (~93% humidity) and were automatically transferred for imaging every hour.

Explant assay

Dissected back skins from E6.5 were placed dermal-side down on transparent PET membrane cell culture inserts with a 0.4-μm pore size (Corning, no. 353090) in six-well plates. Inserts with skins were cultured at 37°C with 5% CO_2 in a humid environment in six-well plates with full media, MMP inhibitor (Sigma, Marimastat, no. 444289, 100 μM), genipin (Sigma, G4796, 50 μM, 250 μM), or SU5402 (10 μM). Genipin is a natural plant extract that has been shown to cross-link extracellular matrix proteins such as collagen and gelatin (*46*), thereby increasing the stiffness of the tissue.

Dense dermal reconstitution assay

Dissociated dermal cells from E8 back skins consisting of three to five rows of emerging follicles were resuspended in full media. Eighteen microliters of full media were added per dissociated skin, and the cells were reconstituted to make a high-density cell solution. Cells were plated in 10-μl drops on cell culture inserts. Commercial agarose beads with 75- to 150-μm diameters were purchased from Bio-Rad (no. 1537302). Homemade agarose beads were made by pipetting 0.6 μl of 0.5% agarose solution (made from agarose powder with low gelling temperature purchased from Sigma, A9045) on a sterile parafilm and letting it polymerize for 5 min. The homemade agarose beads were mixed in the 10-μl drops when indicated. Inserts with cells were cultured at 37°C with 5% CO_2 in a humid environment in six-well plates with full media, FGF (400 ng/ml), or BMP (200 ng/ml).

For all experiments, data include a combination of technical replicates that were performed within a single trial and biological replicates performed across multiple trials. Data from biological replicates and technical replicates were combined if data were consistent. Individual samples from experimental assays were omitted only if initial conditions (e.g., drop geometry, ring geometry) were incorrect owing to technical error.

AFM

Whole embryos from E8 were dissected, rinsed, and immediately transferred to optical cutting temperature compound (OCT) on ice. After two 30-min washes in OCT, they were transferred to embedding molds and snap frozen in ethanol that was precooled with dry ice. Fourteen-micrometer-thick longitudinal frozen sections were obtained by cryosection, transferred to glass-bottom petri dishes (FluoroDish, FD35), and briefly fixed for 5 min in 4% paraformaldehyde for the AFM acquisition (*24*). Acquisition was performed at room temperature using a Nanowizard V (JPK-Bruker) microscope in QITMadvanced Mode (stiffness mapping) or Contact Mode Force Spectroscopy mode (single force curve).

Dense dermal reconstitution cultures treated with full media, FGF (400 ng/ml), or BMP (200 ng/ml) were seeded on 2-mg/ml collagen gel on glass-bottom petri dishes (FluoroDish, FD5040) coated with polylysine (Sigma, P8920) and cultured for 48 hours for the AFM acquisition. Acquisition was performed at 37°C using an MFP-3D-BIO AFM microscope (Oxford Instruments).

Before each experiment, the exact spring constant of the cantilever was determined using the thermal noise method, and its optical sensitivity was determined using a phosphate-buffered saline (PBS)–filled glass-bottom Petri dish as an infinitely stiff surface. The following settings were used: tip Poisson νtip = 0.25, tip Young's modulus Etip = 290 GPa, and sample Poisson νsample = 0.45.

Silicon nitride cantilevers with 5-μm-diameter spherical tips (nominal spring constant k = 0.2 N/m, Bruker) were used for high-resolution stiffness maps. For embryo sections, stiffness maps of 20 μm–by–20 μm, 16-by-16 grid points, and trigger point 1 nN were collected at 1.5 Hz for a single approach-withdraw cycle. One to five measurements were taken per region, per follicle with the following totals: 16 for the core, 19 for the margin, and 25 for the interbud; median values were then obtained. For dense dermal reconstitution, stiffness maps of 90 μm–by–90 μm, 10-by-10 grid points and trigger point 2 to 3 nN were collected at 1.5 Hz for a single approach-withdraw cycle. Four biological replicates per condition were measured. For each biological replicate, five measurements were taken (i.e., 20 data points per condition), and average values were obtained.

A polystyrene particle (45-μm diameter) on a silicon nitride cantilever was used (nominal spring constant k = 0.35 N/m, Novascan) for lower-resolution stiffness curves. For embryo sections, a trigger point of 1 nN was used. Seven follicles were measured. One to six measurements were taken per region per follicle with the following totals: 22 for the core, 21 for the margin, and 32 for the interbud; average values were then obtained. For dense dermal reconstitution, a trigger point of 30 to 50 nN was used to ensure sample penetration of 2 to 3 μm. Four biological replicates per condition were measured. For each biological replicate, 6 to 10 positions were measured. It was measured three times for each position, and average values were obtained.

For high-resolution stiffness maps, the force curve in each grid point was fitted according to the Hertz model (Igor Pro, Wavemetrics) to calculate the Young's modulus. For single force curve measurements, the curve was fitted using the same model. Force curves that did not meet predetermined standards were removed. For embryo sections, the Young's modulus of each region was normalized to the average Young's modulus of the interfollicle region within the same experiment. For the dense dermal reconstitution culture, the Young's modulus for each condition was normalized to the average Young's modulus of the control condition within the same experiment.

MPA

Micropipettes were manufactured as previously described (*13*), except that the pipettes of smallest diameter (<25 μm) were cut using a World Precision Instruments DMF1000 microforge, whereas the larger pipettes (>25 μm) were cut using a Sutter Instrument ceramic tile for scoring glass (NC9569052, Fisher Scientific).

The aspiration apparatus and imaging setup were also previously described (*13*). Dense dermal reconstitution cultures treated with full media, FGF (400 ng/ml), or BMP (200 ng/ml) were each aspirated at various sites using 5- to 7-μm and 50-μm diameter pipettes. For the 5- to 7-μm pipettes, 8 kPa of pressure was applied rapidly at t = 0 s, held constant, and released rapidly at t = 15 s; images were acquired every 1 s from t = 0 s to t = 30 s. In one trial, pressure was held (and released) for 30 rather than 15 s. For the 50-μm pipettes, 4 kPa of pressure was applied at t = 0 s, held until t = 90 s, and then released. Images were acquired every 950 ms for the first 15 s and then every 5 s for the next 75 s, after pressure application and release. Three independent trials (biological replicates) with 6 to 10 technical replicates per trial were measured for the 5- to 7-μm pipette, and three independent trials with five to seven technical replicates per trial were measured for the 50-μm pipette. Homemade agarose beads were aspirated at various sites into a 50-μm diameter pipette under 8 kPa of pressure, applied for 30 s, and then released for 30 s, with images taken every 1 s. Four beads were measured. In every case, the instantaneous strain, creep strain, elastic recovery, and anelastic recovery were captured.

Image analysis was performed as previously described (*13*). The instantaneous strain (i.e., extension of the sample into the pipettes at $t \approx$ 15 s) was used to calculate Young's modulus

Downloaded from https://www.science.org at Rockefeller University on July 10, 2024

for each condition and pipette size. The whole strain curve over time was used to estimate tissue viscoelastic properties, as explained in greater detail in the supplementary text.

TFM

Polyacrylamide (pAA) gels were prepared following previously described methods (*52*). Gels were coated with 40-μg/ml biotin-labeled fibronectin for 2 hours at room temperature before cell seeding. Cells were seeded on gels at a concentration of 670,000 cells/ml in full media, Y27632 (TOCRIS, no. 1254, 10 μM), FGF (400 ng/ml), BMP (100 ng/ml), or LDN (100 nM). The cells were cultured for 18 hours at 37°C with 5% CO_2 in a humid environment before imaging.

To estimate the displacement of the beads caused by cells exerting force on the pAA gels, images of the same region were acquired at two time points: while the cells were seeded on the gels and after adding trypsin to the culture media to detach the cells. Images were collected using an Olympus IX-71 fluorescence microscope with an Andor iXon3 EM-CCD and equipped with a 100×/1.45 NA Plan Apochromat objective (Olympus). Illumination channel 488 nm was used for visualization of the bead layer, whereas cells were visualized using bright-field illumination. MetaMorph for Olympus was used to collect images. For each condition, four to nine independent cultures (biological replicates) with two to six cells per culture were imaged.

The image of beads, while the cells were present, represents the deformed state of the gels, which is compared with its state after the cells have been removed and the gel could relax (zero displacement reference). In FIJI, the images taken at the two time points were aligned using the plug-in "Registration of multichannel timelapse with linear stack alignment with SIFT" to correct for relative translational xy-shift before analyzing the bead displacement with particle image velocimetry (PIV). PIV enables one to interpolate the particle displacements into a regularized grid corresponding to the approximate substrate displacement without the need to track individual bead movements. PIV analysis was conducted using the Matlab toolbox PIVLab (*53*). The displacement vector map generated by PIVlab was used to calculate the traction forces in Matlab. The custom Matlab script implements the unconstrained Fourier transform traction cytometry algorithm described by (*54*). After the stress fields were calculated, the cell boundaries of an individual cell were outlined manually. Stress vectors inside of the cell boundaries that surpassed the background threshold (defined as the average stress magnitude of vectors in an area without cells) were used to calculate the average and maximum stress magnitude inside of the cell boundaries. A one-way analysis of variance (ANOVA) Welch and Brown-Forsythe test was performed to compare the mean of each condition with that of the control condition.

SEM

Cell-culture insert membranes from dense dermal reconstitution assays treated with full media, FGF (400 ng/ml), or BMP (200 ng/ml) were cut in the shape of round disks of 10-mm diameter. Each disk was placed in individual well of a cell-culture plate, and the cells were fixed in 2% glutaraldehyde, 4% paraformaldehyde in 0.1M sodium cacodylate buffer, pH 7.2 for 2 hours at room temperature followed by overnight fixation at 4°C. The cells were then washed three times with 0.1-M sodium cacodylate, pH 7.2 for 5 min each. They were then treated with 1% osmium tetroxide in 0.1-M sodium cacodylate buffer, pH 7.2 for 45 min at 4°C. After washing with Milli-Q water, cells were dehydrated in a graded ethanol series. Dehydration of cells with 30, 50, and 70% ethanol were performed at 4°C, whereas 90 and 100% ethanol treatments were performed at room temperature. Cells were dried using an Autosamdri-931 (Tousimis, USA) critical point dryer (CPD). The detailed CPD protocol was as follows: slow fill 3 min, fill time 6 min, purge time 10 min, postpurge 4 min, critical point 10 min, and bleed/vent 300 psi. After CPD, the cells were mounted on carbon tape adhered to a flat stub. The cells were coated with a 9-nm-thick iridium layer using a Leica EM AC600 sputter coater (Leica, USA). The coated samples were imaged with a JEOL JSM-IT500HR scanning electron microscope (Jeol, Inc., USA). Six independent cultures per condition were imaged.

Immunohistochemistry and imaging

Skin samples for whole-mount imaging were collected at the appropriate embryonic day and fixed in 4% paraformaldehyde in PBS at room temperature for 1 hour. After fixation, samples were rinsed in PBS and PBS-Triton (PBSTrHI, 1.0% Triton X-100) and then blocked immediately for 1 hour in 100% CAS Block (Invitrogen).

Skin samples shown in cross section were from whole embryos at the appropriate embryonic day fixed in 4% paraformaldehyde in PBS overnight at 4°C. Wild-type skins and skins with the epidermis removed (shown in Fig. 6) were dissected from embryos at the appropriate embryonic day and immediately fixed in 4% paraformaldehyde in PBS at room temperature for 1 hour. They were then embedded in OCT. Fourteen-micrometer-thick longitudinal or transverse frozen sections were obtained for immunofluorescence, rinsed in PBS and PBS-Triton (PBSTrLO, 0.1% Triton X-100), and then blocked immediately for 30 min in 100% CAS Block.

Collagen-cell disks were fixed in 4% paraformaldehyde in PBS for 30 min at room temperature. Explant cultures were fixed in 4% paraformaldehyde in PBS for 1 hour at room temperature. Dense dermal reconstitution cultures were fixed in 4% paraformaldehyde in PBS for 30 min at room temperature. After fixation, samples were rinsed in PBS and PBS-Triton (PBSTrHI, 1.0% Triton X-100) and then blocked immediately for 1 hour in 100% CAS Block.

After blocking, all samples were stained in 10% CAS in PBSTrLO overnight at 4°C. The following primary antibodies were used: laminin (1:100 sections; ab11575 Abcam), E-cadherin (1:100 sections; ab76055 Abcam), fibronectin (1:100 wholemount; ab6328 Abcam), pSMAD1/5/9 (1:300 sections; 1:100 whole-mount; 13820 Cell Signaling Technologies), and pERK (1:100 sections; sc-7383 Santa Cruz Biotechnology). Samples were subsequently rinsed in PBSTr LO and then incubated for 2 hours with the following secondary antibodies: Alexa Fluor 488 (1:300, Invitrogen), Alexa Fluor 555 (1:300, Invitrogen), and Alexa Fluor 647 (1:300, Invitrogen). 4′,6-Diamidino-2-phenylindole (DAPI) (1:1000, Invitrogen) was used to stain nuclei. Alexa Fluor 488 and 647 Phalloidin (Fisher Scientific, A12379, A22287) were used to stain actin. Antigen retrieval was used for pSMAD and pERK staining.

For FISH, skin sections were postfixed in 4% paraformaldehyde in PBS, permeabilized through an ethanol series (50, 70, and 100%, 5 min each) at −20°C, and rinsed in PBS with Tween (PBST) (0.1% Tween-20). Probe hybridization and amplification were performed using a protocol from Molecular Instruments (*55*). The probes for *postn*, *jam3*, *mmp27*, *fat4*, *zfhx3*, *ppp1r14b*, and *fst* were designed and produced by Molecular Instruments.

Longitudinal sections shown in Fig. 1, wholemount images of fixed skin explants shown in Figs. 1 and 2, and immunofluorescent images of collagen-cell disks shown in Fig. 5 were imaged using a Zeiss LSM880 and are max-intensity projections of two to three *z*-stacks. All other imaging was performed using a Zeiss AxioImager.

Analysis and quantification

Nuclear aspect ratio and density were quantified in ImageJ (*56*). The number of nuclei in each respective region was counted and normalized per 500-μm^2 area.

Intensity values for the core and margin in Fig. 2 were sampled from three regions per domain per embryo, and all values are plotted. The intensity values in Fig. 2 were normalized (background subtraction) to a region outside the core and margin domains. To account for variation in fibronectin intensity between samples in Fig. 5, we first normalized both raw fibronectin and DAPI immunofluorescent signals for the entire region of interest (ROI) to the fluorescence intensity in a region within the disk with no cells or matrix. We then divided the

Downloaded from https://www.science.org at Rockefeller University on July 10, 2024

fibronectin normalized value by the DAPI normalized value. Together, this reduced variability that was caused by immunofluorescence as well as by changes in cell density.

Measurements for aspect ratio, area, circularity, and average intensity values were performed in ImageJ. Measurements for contact length and interspheroid (intersphere) angle were performed as previously described (*39*).

Directionality measurements were made using the Directionality plug-in in ImageJ. A 100-μm–by–100-μm ROI was analyzed using the Fourier components method. For measurements showing alignment along beads, ROIs were measured such that 0° was equal to the line tangent to the bead and 90° was radially oriented away from the bead. To determine the "fraction aligned," measurements from 0° to 30° were binned. Directionality measurements were plotted using matplotlib in Python.

All other measurements and statistical analyses were performed in Prism. Box plots show min-max distribution. When calculated, p values were determined using a Student's t test with Welch's correction (except for the TFM results, which were specified in the TFM section above).

Single-cell RNA sequencing

Dissociated dermal cells from E8 back skins consisting of three to five rows of emerging follicles were processed using a 10X Genomics v3 kit, and libraries were sequenced on Illumina Nextseq 500 system at the Genomics Resource Center at the Rockefeller University. Raw sequencing reads were uploaded to the NCBI Sequence Read Archive (SRA, PRJNA926968).

Sequenced reads were processed using Cellranger version 6.0 (10X Genomics). The reads were mapped to chicken genome (Galgal 6), and the counting matrices were generated. We identified 7990 cells. The mean read per cell was 22,981, and the median number of genes in each cell was 967. Ambient RNA interferences were estimated and removed using SoupX (*57*) by the default setting. Doublets and multiple cells in single droplet were identified and removed using Scrublet (*58*). Corrected matrices were loaded as a Seurat (v4.0) (*59*) object. Using Seurat, cells with fewer than 200 gene expression or with a percentage of mitochondrial reads greater than 20% were removed; the gene expression of cells was normalized with scale factor 1000, and the top-3000 variable features of each object were identified with the "vst" method.

The remaining 6355 cells were used for dimensional reduction, projection, and clustering analysis. Five clusters were identified from the initial clustering analysis. Cell type–specific gene sets were built based on a single-cell mRNA sequencing dataset of human skin (*60*) to annotate the clusters. On the basis of gene set enrichment analysis (GSEA) (*61*) and the marker genes of each cluster, these were identified as fibroblast, blood cell, vascular endothelial cell, muscle cell, and immune cell (fig. 2A and data S1). The remaining 5829 fibroblasts were reclustered. A population of subjacent dermal cells with marker gene ZFHX3 expression was identified (fig. S2B). The remaining 4373 superficial dermal cells were reclustered. A cell cycle highly related cluster was identified based on GSEA using cell cycle–related gene sets from MsigDB (C2-CP gene sets), and the marker gene of this population was expressed uniformly in the superficial dermis (fig. S2C and data S2). Therefore, we concluded that this cluster did not correlate to any cell population with a specific spatial pattern but rather to a cell cycle state among all cells in the superficial dermis. After removing this cell cycle highly related cluster, the remaining 2199 cells were reclustered. Cluster stability analysis was performed, and the optimal resolution of 0.2 was used. Four clusters were identified (fig. S2D).

Simulations

The full details of the mathematical model, including discussion of equations of motion, boundary conditions, numerical details, and parameter choices, can be found in the supplementary text. The code related to the mathematical model and simulations has been uploaded to Zenodo (*62*). In summary, we adopted a continuum model of the dermal-epidermal deformation as an active multiphase viscoelastic flow. Our choice of a continuum model is motivated by our primary interest in understanding the interaction of aggregates of cells—by choosing to coarse grain, we can more easily study the broad effect of material differences between different tissue layers. In particular, we identified five relevant regions on the basis of our experimental analysis (Fig. 6): the follicle epidermis (yellow), the core dermal condensate (orange), the condensate margin (dark blue), the deep dermal tissue (light blue), and the extratissue fluid external to the epidermis (black). We treated the matter that makes up each region as a distinct material phase and examined their mechanical interactions with a Cahn-Hilliard style phase-field model coupled to equations for force balance, strain evolution, and other relevant mechanical fields (*63*, *64*). In our model, the epidermis is a relatively stiff viscous solid. By contrast, the dermal tissues are assigned substantially weaker elastic moduli and feature internal relaxation consistent with remodeling of fluidized tissue. Because our experiments suggest that anisotropic contractility of the margin dermal cells drives deformation, we assigned an active nematic stress to the boundary phase. The orientation of this stress is dependent on a nematic field anchored to the phase boundaries such that it is parallel to the borders between dermal regions and perpendicular to the basement membrane; we based this choice on observed elongation of dermal cells along this direction. Finally, we treated extratissue fluid as a passive viscous fluid.

In the interest of simplicity, we assumed that the mechanical effect of the basement membrane can be lumped into the stiffness of the epidermis. To simulate the empirically observed basement membrane weakening, we approximated the weakening of the basement membrane by applying a localized soft spot along the interface between the core dermis and epidermis, which we found generates consistent changes in deformation as experimental perturbations of the basement membrane. As expressed in greater detail in the supplementary text, wherever possible, parameters were chosen on the basis of our own experiments. All simulations were conducted with the Dedalus (v3) (*65*) spectral framework for partial differential equations on a paralleled 512-by-512 square mesh, with boundary conditions listed in the supplementary text. Although the real system is three dimensional, we consistently found that a planar representation of our model generated sufficiently good matches with experimental observations.

Perturbations to simulation parameters were used to test the extent to which our phase-field model captured the experimental system. Tissue stiffness (Fig. 6E) was tuned to be two or five times that of the baseline condition. Epidermis removal simulations (Fig. 6F) were performed such that the effect of the epidermis phase was removed. For perturbations to model the effects of inhibiting MMPs (Fig. 6G), the simulated effect of weakening the core dermis–epidermis boundary was removed. To model the effect of contractility in our system (fig. S7A), contractility was reduced by 1/2 or 1/10 in our simulations. Simulations are shown as movies and as time points in the supplementary text. In addition, simulations of the spheroid merger experiments were performed using the same model but in each case featuring only disks that matched the initial geometry and material properties of a particular dermal phase in our experiments. In each case, the spheres were allowed to merge under the passive effects of surface tension for 20 hours. We were able to estimate the viscoelastic relaxation timescales associated with each dermal phase by tuning parameters in each case until a close morphological match with experiments was determined.

REFERENCES AND NOTES

1. W. Driever, C. Nüsslein-Volhard, A gradient of bicoid protein in *Drosophila* embryos. *Cell* **54**, 83–93 (1988). doi: 10.1016/0092-8674(88)90182-1; pmid: 3383244
2. E. Laufer, C. E. Nelson, R. L. Johnson, B. A. Morgan, C. Tabin, Sonic hedgehog and Fgf-4 act through a signaling cascade and feedback loop to integrate growth and patterning of the developing limb bud. *Cell* **79**, 993–1003 (1994). doi: 10.1016/0092-8674(94)90030-2; pmid: 8001146

Downloaded from https://www.science.org at Rockefeller University on July 10, 2024

3. Y. Chen, A. F. Schier, The zebrafish Nodal signal Squint functions as a morphogen. *Nature* **411**, 607–610 (2001). doi: 10.1038/35079121; pmid: 11385578
4. A. M. Turing, The chemical basis of morphogenesis. *Bull. Math. Biol.* **52**, 153–197 (1990). doi: 10.1016/S0092-8240(05)80008-4; pmid: 2185858
5. L. Wolpert, Positional information and pattern formation. *Curr. Top. Dev. Biol.* **6**, 183–224 (1971). doi: 10.1016/S0070-2153(08)60641-9; pmid: 4950136
6. N. Serrano, P. H. O'Farrell, Limb morphogenesis: Connections between patterning and growth. *Curr. Biol.* **7**, R186–R195 (1997). doi: 10.1016/S0960-9822(97)70085-X; pmid: 9162486
7. L. C. Biggs *et al*., Hair follicle dermal condensation forms via Fgf20 primed cell cycle exit, cell motility, and aggregation. *eLife* **7**, e36468 (2018). doi: 10.7554/eLife.36468; pmid: 30063206
8. J. D. Murray, G. F. Oster, A. K. Harris, A mechanical model for mesenchymal morphogenesis. *J. Math. Biol.* **17**, 125–129 (1983). doi: 10.1007/BF00276117; pmid: 6875405
9. P. Alberch, "Developmental constraints in evolutionary processes" in *Evolution and Development*, J. T. Bonner, Ed., Dahlem Workshop Report series, vol. 22 (Springer, 1982), pp. 313–332.doi: 10.1007/978-3-642-45532-2_15
10. P. F. Lenne *et al*., Roadmap for the multiscale coupling of biochemical and mechanical signals during development. *Phys. Biol.* **18**, 041501 (2021). doi: 10.1088/1478-3975/abd0db; pmid: 33276350
11. H. S. Jung *et al*., Local inhibitory action of BMPs and their relationships with activators in feather formation: Implications for periodic patterning. *Dev. Biol.* **196**, 11–23 (1998). doi: 10.1006/dbio.1998.8850; pmid: 9527877
12. A. E. Shyer *et al*., Emergent cellular self-organization and mechanosensation initiate follicle pattern in the avian skin. *Science* **357**, 811–815 (2017). doi: 10.1126/science.aai7868; pmid: 28705989
13. K. H. Palmquist *et al*., Reciprocal cell-ECM dynamics generate supracellular fluidity underlying spontaneous follicle patterning. *Cell* **185**, 1960–1973.e11 (2022). doi: 10.1016/j.cell.2022.04.023; pmid: 35551765
14. H. M. Phillips, M. S. Steinberg, Embryonic tissues as elasticoviscous liquids. I. Rapid and slow shape changes in centrifuged cell aggregates. *J. Cell Sci.* **30**, 1–20 (1978). doi: 10.1242/jcs.30.1.1; pmid: 649680
15. F. Michon, L. Forest, E. Collomb, J. Demongeot, D. Dhouailly, BMP2 and BMP7 play antagonistic roles in feather induction. *Development* **135**, 2797–2805 (2008). doi: 10.1242/dev.018341; pmid: 18635609
16. C. M. Lin, T. X. Jiang, R. B. Widelitz, C. M. Chuong, Molecular signaling in feather morphogenesis. *Curr. Opin. Cell Biol.* **18**, 730–741 (2006). doi: 10.1016/j.ceb.2006.10.009; pmid: 17049829
17. C. F. Drew *et al*., The Edar subfamily in feather placode formation. *Dev. Biol.* **305**, 232–245 (2007). doi: 10.1016/j.ydbio.2007.02.011; pmid: 17362907
18. K. J. Painter, W. Ho, D. J. Headon, A chemotaxis model of feather primordia pattern formation during avian development. *J. Theor. Biol.* **437**, 225–238 (2018). doi: 10.1016/j.jtbi.2017.10.026; pmid: 29097151
19. M. Scaal *et al*., BMPs induce dermal markers and ectopic feather tracts. *Mech. Dev.* **110**, 51–60 (2002). doi: 10.1016/S0925-4773(01)00552-4; pmid: 11744368
20. M. Mandler, A. Neubüser, FGF signaling is required for initiation of feather placode development. *Development* **131**, 3333–3343 (2004). doi: 10.1242/dev.01203; pmid: 15201222
21. H. Song, Y. Wang, P. F. Goetinck, Fibroblast growth factor 2 can replace ectodermal signaling for feather development. *Proc. Natl. Acad. Sci. U.S.A.* **93**, 10246–10249 (1996). doi: 10.1073/pnas.93.19.10246; pmid: 8816784
22. S. Noramly, B. A. Morgan, BMPs mediate lateral inhibition at successive stages in feather tract development. *Development* **125**, 3775–3787 (1998). doi: 10.1242/dev.125.19.3775; pmid: 9729486
23. K. Patel, H. Makarenkova, H. S. Jung, The role of long range, local and direct signalling molecules during chick feather bud development involving the BMPs, follistatin and the Eph receptor tyrosine kinase Eph-A4. *Mech. Dev.* **86**, 51–62 (1999). doi: 10.1016/S0925-4773(99)00107-0; pmid: 10446265
24. A. Calò *et al*., Spatial mapping of the collagen distribution in human and mouse tissues by force volume atomic force microscopy. *Sci. Rep.* **10**, 15664 (2020). doi: 10.1038/s41598-020-72564-9; pmid: 32973235
25. C. S. Campbell, Granular material flows–an overview. *Powder Technol.* **162**, 208–229 (2006). doi: 10.1016/j.powtec.2005.12.008
26. J. Heemskerk, S. DiNardo, R. Kostriken, P. H. O'Farrell, Multiple modes of engrailed regulation in the progression towards cell fate determination. *Nature* **352**, 404–410 (1991). doi: 10.1038/352404a0; pmid: 1861720
27. A. Warmflash, B. Sorre, F. Etoc, E. D. Siggia, A. H. Brivanlou, A method to recapitulate early embryonic spatial patterning in human embryonic stem cells. *Nat. Methods* **11**, 847–854 (2014). doi: 10.1038/nmeth.3016; pmid: 24973948
28. M. Weaver, N. R. Dunn, B. L. Hogan, Bmp4 and Fgf10 play opposing roles during lung bud morphogenesis. *Development* **127**, 2695–2704 (2000). doi: 10.1242/dev.127.12.2695; pmid: 10821767
29. B. Bénazéraf *et al*., A random cell motility gradient downstream of FGF controls elongation of an amniote embryo. *Nature* **466**, 248–252 (2010). doi: 10.1038/nature09151; pmid: 20613841
30. A. Mongera *et al*., A fluid-to-solid jamming transition underlies vertebrate body axis elongation. *Nature* **561**, 401–405 (2018). doi: 10.1038/s41586-018-0479-2; pmid: 30185907
31. N. I. Petridou, S. Grigolon, G. Salbreux, E. Hannezo, C. P. Heisenberg, Fluidization-mediated tissue spreading by mitotic cell rounding and non-canonical Wnt signalling. *Nat. Cell Biol.* **21**, 169–178 (2019). doi: 10.1038/s41556-018-0247-4; pmid: 30559456
32. J. W. Spurlin III *et al*., Mesenchymal proteases and tissue fluidity remodel the extracellular matrix during airway epithelial branching in the embryonic avian lung. *Development* **146**, dev175257 (2019). doi: 10.1242/dev.175257; pmid: 31371376
33. K. Guevorkian, M. J. Colbert, M. Durth, S. Dufour, F. Brochard-Wyart, Aspiration of biological viscoelastic drops. *Phys. Rev. Lett.* **104**, 218101 (2010). doi: 10.1103/PhysRevLett.104.218101; pmid: 20867138
34. K. A. Shorlin, J. R. de Bruyn, M. Graham, S. W. Morris, Development and geometry of isotropic and directional shrinkage-crack patterns. *Phys. Rev. E Stat. Phys. Plasmas Fluids Relat. Interdiscip. Topics* **61**, 6950–6957 (2000). doi: 10.1103/PhysRevE.61.6950; pmid: 11088387
35. Y. Shin, C. P. Brangwynne, Liquid phase condensation in cell physiology and disease. *Science* **357**, eaaf4382 (2017). doi: 10.1126/science.aaf4382; pmid: 28935776
36. S. Alberti *et al*., A user's guide for phase separation assays with purified proteins. *J. Mol. Biol.* **430**, 4806–4820 (2018). doi: 10.1016/j.jmb.2018.06.038; pmid: 29944854
37. K. Jakab *et al*., Relating cell and tissue mechanics: Implications and applications. *Dev. Dyn.* **237**, 2438–2449 (2008). doi: 10.1002/dvdy.21684; pmid: 18729216
38. S. Douezan, F. Brochard-Wyart, Active diffusion-limited aggregation of cells. *Soft Matter* **8**, 784–788 (2012). doi: 10.1039/C1SM06399E
39. M. J. Susienka, B. T. Wilks, J. R. Morgan, Quantifying the kinetics and morphological changes of the fusion of spheroid building blocks. *Biofabrication* **8**, 045003 (2016). doi: 10.1088/1758-5090/8/4/045003; pmid: 27721222
40. J. Zhou, H. Y. Kim, J. H. Wang, L. A. Davidson, Macroscopic stiffening of embryonic tissues via microtubules, RhoGEF and the assembly of contractile bundles of actomyosin. *Development* **137**, 2785–2794 (2010). doi: 10.1242/dev.045997; pmid: 20630946
41. D. E. Discher, P. Janmey, Y. L. Wang, Tissue cells feel and respond to the stiffness of their substrate. *Science* **310**, 1139–1143 (2005). doi: 10.1126/science.1116995; pmid: 16293750
42. M. G. Mendez, D. Restle, P. A. Janmey, Vimentin enhances cell elastic behavior and protects against compressive stress. *Biophys. J.* **107**, 314–323 (2014). doi: 10.1016/j.bpj.2014.04.050; pmid: 25028873
43. K. Pogoda *et al*., Unique role of vimentin networks in compression stiffening of cells and protection of nuclei from compressive stress. *Nano Lett.* **22**, 4725–4732 (2022). doi: 10.1021/acs.nanolett.2c00736; pmid: 35678828
44. C. E. Caicedo-Carvajal, T. Shinbrot, R. A. Foty, α5β1 integrin-fibronectin interactions specify liquid to solid phase transition of 3D cellular aggregates. *PLOS ONE* **5**, e11830 (2010). doi: 10.1371/journal.pone.0011830; pmid: 20686611
45. E. A. Lenselink, Role of fibronectin in normal wound healing. *Int. Wound J.* **12**, 313–316 (2015). doi: 10.1111/iwj.12109; pmid: 23742140
46. H. G. Sundararaghavan *et al*., Genipin-induced changes in collagen gels: Correlation of mechanical properties to fluorescence. *J. Biomed. Mater. Res. A* **87A**, 308–320 (2008). doi: 10.1002/jbm.a.31715; pmid: 18181104
47. N. Saxena, K. W. Mok, M. Rendl, An updated classification of hair follicle morphogenesis. *Exp. Dermatol.* **28**, 332–344 (2019). doi: 10.1111/exd.13913; pmid: 30887615
48. D. Pinheiro, R. Kardos, É. Hannezo, C. P. Heisenberg, Morphogen gradient orchestrates pattern-preserving tissue morphogenesis via motility-driven unjamming. *Nat. Phys.* **18**, 1482–1493 (2022). doi: 10.1038/s41567-022-01787-6
49. D. Bi, X. Yang, M. C. Marchetti, M. L. Manning, Motility-driven glass and jamming transitions in biological tissues. *Phys. Rev. X* **6**, 021011 (2016). doi: 10.1103/PhysRevX.6.021011; pmid: 28966874
50. D. T. McSwiggen, M. Mir, X. Darzacq, R. Tjian, Evaluating phase separation in live cells: Diagnosis, caveats, and functional consequences. *Genes Dev.* **33**, 1619–1634 (2019). doi: 10.1101/gad.331520.119; pmid: 31594803
51. V. Hamburger, H. L. Hamilton, A series of normal stages in the development of the chick embryo. *Dev. Dyn.* **195**, 231–272 (1992). doi: 10.1002/aja.1001950404; pmid: 1304821
52. D. J. Yuan, L. Shi, L. C. Kam, Biphasic response of T cell activation to substrate stiffness. *Biomaterials* **273**, 120797 (2021). doi: 10.1016/j.biomaterials.2021.120797; pmid: 33878536
53. W. Thielicke, R. Sonntag, Particle Image Velocimetry for MATLAB: Accuracy and enhanced algorithms in PIVlab. *J. Open Res. Softw.* **9**, 12 (2021). doi: 10.5334/jors.334
54. J. P. Butler, I. M. Tolić-Nørrelykke, B. Fabry, J. J. Fredberg, Traction fields, moments, and strain energy that cells exert on their surroundings. *Am. J. Physiol. Cell Physiol.* **282**, C595–C605 (2002). doi: 10.1152/ajpcell.00270.2001; pmid: 11832345
55. H. M. T. Choi *et al*., Third-generation *in situ* hybridization chain reaction: Multiplexed, quantitative, sensitive, versatile, robust. *Development* **145**, dev165753 (2018). doi: 10.1242/dev.165753; pmid: 29945988
56. C. A. Schneider, W. S. Rasband, K. W. Eliceiri, NIH Image to ImageJ: 25 years of image analysis. *Nat. Methods* **9**, 671–675 (2012). doi: 10.1038/nmeth.2089; pmid: 22930834
57. M. D. Young, S. Behjati, SoupX removes ambient RNA contamination from droplet-based single-cell RNA sequencing data. *Gigascience* **9**, giaa151 (2020). doi: 10.1093/gigascience/giaa151; pmid: 33367645
58. S. L. Wolock, R. Lopez, A. M. Klein, Scrublet: Computational identification of cell doublets in single-cell transcriptomic data. *Cell Syst.* **8**, 281–291.e9 (2019). doi: 10.1016/j.cels.2018.11.005; pmid: 30954476
59. Y. Hao *et al*., Integrated analysis of multimodal single-cell data. *Cell* **184**, 3573–3587.e29 (2021). doi: 10.1016/j.cell.2021.04.048; pmid: 34062119
60. L. Solé-Boldo *et al*., Single-cell transcriptomes of the human skin reveal age-related loss of fibroblast priming. *Commun. Biol.* **3**, 188 (2020). doi: 10.1038/s42003-020-0922-4; pmid: 32327715
61. A. Subramanian *et al*., Gene set enrichment analysis: A knowledge-based approach for interpreting genome-wide expression profiles. *Proc. Natl. Acad. Sci. U.S.A.* **102**, 15545–15550 (2005). doi: 10.1073/pnas.0506580102; pmid: 16199517
62. P. Miller, Code Repository: Morphogens enable interacting supracellular phases that generate organ architecture (v0.9). Zenodo (2023); https://doi.org/10.5281/zenodo.8348004.
63. D. M. Anderson, G. B. McFadden, A. A. Wheeler, Diffuse-interface methods in fluid mechanics. *Annu. Rev. Fluid Mech.* **30**, 139–165 (1998). doi: 10.1146/annurev.fluid.30.1.139
64. J. Kim, Phase-field models for multi-component fluid flows. *Commun. Comput. Phys.* **12**, 613–661 (2012). doi: 10.4208/cicp.301110.040811a
65. K. J. Burns, G. M. Vasil, J. S. Oishi, D. Lecoanet, B. P. Brown, Dedalus: A flexible framework for numerical simulations with spectral methods. *Phys. Rev. Res.* **2**, 023068 (2020). doi: 10.1103/PhysRevResearch.2.023068

ACKNOWLEDGMENTS

We thank members of the Laboratory of Morphogenesis at The Rockefeller University for discussion and feedback on the manuscript and L. Marraffini and L. Hoffman for comments on the manuscript and/or helpful discussions. We thank the Rockefeller University's shared Bio-Imaging Resource Center for technical support and microscope use, the Rockefeller University Genomics Core Facility for performing single-cell RNA sequencing, T. Carroll and J.-D. Luo of the Rockefeller University Bioinformatics Resource Center for the processing and initial analysis of single-cell RNA sequencing data, A. Pasolli and the Electron Microscopy Resource Center for technical support and consultation, and Y. Romin and the Molecular Cytology Core Facility at Memorial Sloan Kettering Cancer Center for consultation, imaging, and analysis. **Funding:** This work was funded by the Burroughs Wellcome Foundation (A.E.S.), the Irma T. Hirschl Foundation (A.E.S.), the Alfred P. Sloan Foundation, an Innovate Award (A.E.S.), the Searle Scholars Program (A.E.S.), an NSF National Graduate Research Fellowship (K.H.P.), NIH grant R21AI150244 (L.C.K.), and NIH grant P30 CA008748 (Memorial Sloan

Downloaded from https://www.science.org at Rockefeller University on July 10, 2024

Kettering Cancer Center, Molecular Cytology Core Facility). **Author contributions:** P.W.M., A.E.S., and A.R.R. are senior authors. A.R.R. and A.E.S. conceived of the project with input from S.Y. and K.H.P. A.R.R., A.E.S., S.Y., and K.H.P. developed assays, designed experiments, and interpreted results. S.Y. and K.H.P. performed experiments and analyzed data. L.N. assisted with assay development, performed experiments, and analyzed data. C.R.P. performed MPA experiments, advised on data analysis, and consulted on the data interpretation. P.J.S. performed TFM and conducted the analysis with assistance and advice from L.C.K. A.S. performed the SEM experiments and imaging. P.W.M. developed the theoretical model and simulations. A.R.R. and A.E.S. wrote the original draft of the manuscript with input and editing from S.Y., K.H.P., and P.W.M. All authors discussed the results and implications and commented on the manuscript at all stages. **Competing interests:** The authors declare that they have no competing interests. **Data and materials availability:** Raw sequencing reads were uploaded to the NCBI Sequence Read Archive (SRA) under accession number PRJNA926968. All data are available in the manuscript and the supplementary materials, and the code related to the mathematical model and simulations is available at Zenodo (*62*). **License information:** Copyright © 2023 the authors, some rights reserved; exclusive licensee American Association for the Advancement of Science. No claim to original US government works. https://www.science.org/about/science-licenses-journal-article-reuse

SUPPLEMENTARY MATERIALS

science.org/doi/10.1126/science.adg5579
Supplementary Text
Figs. S1 to S7
References (*66*–*80*)
MDAR Reproducibility Checklist
Movies S1 to S8
Data S1 and S2

Submitted 26 January 2023; resubmitted 18 July 2023
Accepted 27 September 2023
10.1126/science.adg5579

Downloaded from https://www.science.org at Rockefeller University on July 10, 2024